Corner problems and global accuracy in the boundary element solution of nonlinear wave flows

S. T. Grilli and I. A. Svendsen

Center for Applied Coastal Research, Department of Civil Engineering University of Delaware, Newark, DE 19716, USA

The numerical model for nonlinear wave propagation in the physical space, developed by Grilli, *et al.*[12,13], uses a higher-order BEM for solving Laplace's equation, and a higher-order Taylor expansion for integrating in time the two nonlinear free surface boundary conditions. The corners of the fluid domain were modelled by double-nodes with imposition of potential continuity. Nonlinear wave generation, propagation and runup on slopes were successfully studied with this model. In some applications, however, the solution was found to be somewhat inaccurate in the corners and this sometimes led to wave instability after propagation in time.

In this paper, global and local accuracy of the model are improved by using a more stable free surface representation based on quasi-spline elements and an improved corner solution combining the enforcement of compatibility relationships in the double-nodes with an adaptive integration which provides almost arbitrary accuracy in the BEM numerical integrations. These improvements of the model are systematically checked on simple examples with analytical solutions. Effects of accuracy of the numerical integrations, convergence with refined discretization, domain aspect ratio in relation with horizontal and vertical grid steps, are separately assessed. Global accuracy of the computations with the new corner solution is studied by solving nonlinear water wave flows in a two-dimensional numerical wavetank. The optimum relationship between space and time discretization in the model is derived from these computations and expressed as an optimum Courant number of ~0.5. Applications with both exact constant shape waves (solitary waves) and overturning waves generated by a piston wavemaker are presented in detail.

Key words: boundary element method; nonlinear water waves. Free surface flows; breaking waves; piston wavemaker; corner problems; flow singularities; spline elements; solitary waves

1. INTRODUCTION

Over the last decade numerical solution of the exact nonlinear equations for the inviscid water waves using a Boundary Integral Equation (BIE) description has become an extremely successful method. Most of the previous contributions, however, utilize space periodicity of the waves and also are based on a conformal mapping of physical space onto a plane in which the equivalent of the free surface is the only part left of the boundary. The BIE is then solved in the transformed plane. There are many advantages of this method which have been explored extensively by many authors (see Longuet-Higgins and Cokelet[24], Vinje and Brevig[33] and Dold and Peregrine[5]; for a more complete literature survey, see Grilli, *et al.*[13]). The procedure, however, also has some important limitations which are associated with the use of complex variables and with the assumption of waves that are periodic in space.

To be able to address more general water wave problems, we developed an alternative method, where we considered the wave motion in the physical space (Grilli, *et al.*[12,13]; Grilli and Svendsen[14,15,16]). We used the BEM for solving Laplace's equation, and a higher-order Taylor expansion for integrating in time the two nonlinear free surface boundary conditions. Nonlinear wave generation, propagation and runup on slopes and interaction with other coastal structures (like submerged breakwaters) can successfully be studied with this model. Various ways of generating the waves include numerical piston or flap wavemakers (Grilli, *et al.*[12,13]; Grilli and Svendsen[14,16,17]), internal sources (Grilli and Svendsen[15]) and the imposition of an initial wave potential on the free surface (Grilli, *et al.*[12]; Grilli and Svendsen[18]). Nonlinear wave absorption was also addressed (Grilli, *et al.*[13]).

The present paper first examines the problems associated with the corners in the fluid domain where the free surface and bottom boundaries intersect the lateral boundaries (A to D, Fig. 1). Such corners can be avoided in the above mentioned approaches based on conformally mapped space and wave periodicity. The corners usually separate parts of the boundary with different boundary conditions. In our previous studies, all corners of the fluid domain were modelled by double-nodes with imposition of potential continuity, and we will continue to do so. In some applications, however, the solution was found to be somewhat inaccurate in the corners and this

 © 1990 Computational Mechanics Publications

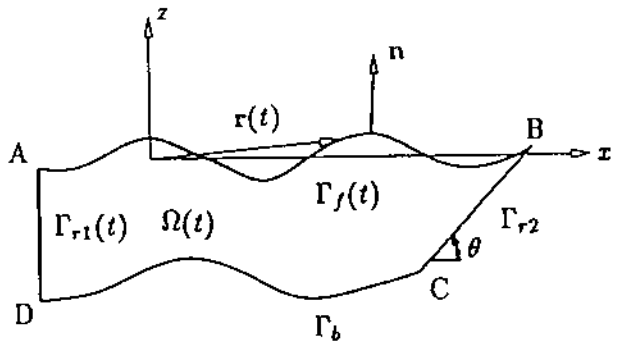

Fig. 1. Computational domain $\Omega(t)$ for the BEM, with four corners A to D. $\Gamma_f(t)$ is the free surface, Γ_b the bottom, $\Gamma_{r1}(t)$ the wave generator and Γ_{r2} a fixed slope of angle θ.

sometimes led to wave instability after propagation in time.

The loss of accuracy in the corners has been pointed out by many authors using the BEM for solving Laplace's equation with mixed Dirichlet-Neumann boundary conditions. However, many authors only discuss the corner issues rather vaguely and it is often difficult to assess which of the many problems have been properly addressed in their solution procedure. In the following, we list five independent aspects of this problem which we think have not quite been well identified, in the literature.

1. The first deals with the exact mathematical solution in the corners of the equations which we solve approximately by the BEM. To analyze the exact solution, one has to consider both the Laplace equation and its time dependent nonlinear boundary conditions. In our problem, in particular, the actual solution may become singular in the corners under some particular boundary conditions (e.g., impulsive wavemaker motion). This is discussed in Section 4.1 and can be named, in short: *possible corner singularity of the exact mathematical solution.*
2. Even if the exact mathematical solution of the nonlinear flow equations is singular in the corners, the numerical solution only approximates the exact solution by a combination of the functions *a priori* selected in the numerical model for representing the solution between the collocation nodes. In the case of the BEM, for instance, if the potential is modelled on the free surface by a piecewise polynomial approximation (shape functions or splines within each boundary element), the numerical solution close to the corner will never become anything but a polynomial variation. In particular, a logarithmic singularity cannot be represented in the numerical results (even if it actually exists). If, in a given problem, the corner singularity of the solution is analytically derived to a leading order, it must be represented in a BEM approximation by using the equivalent singular function as a shape function in the last element close to the corner, with proper numerical integration. This technique of "singular elements" has proved very successful in such fields as fracture mechanics. This aspect can be named, in short: *removal of the actual corner singularity* (as done by Cointe[3], for some weakly nonlinear water wave problems).
3. A purely numerical aspect, is the accuracy of the numerical integrations, close to the corner. In the BEM using higher-order elements, both regular and weakly singular integrals are always evaluated with great care and sophistication, when the observation points belongs to the integrated element. When it does not belong to the element, however, simple integrations (e.g., Gauss quadrature) are usually used. In our model, we observe important losses of accuracy of these regular integrals in situations where the observation point, though not on the element, becomes quite close to it. It turned out, the variations of the BIE kernels over the element are too rapid in this case, to be accurately represented by a reasonable number of so-called Gauss points. Such situations occur, in particular, when the elements close to the corners of the fluid domain are integrated with respect to nodes on the other side of the corner, but also when the distance between two boundaries tends to vanish (e.g. in the narrow wedge that develops during wave rundown on a slope). A very poor corner solution in the BEM always results from these local losses of accuracy (associated to an overall average loss of accuracy of the solution) which, we believe, some authors may have misinterpreted as being due to some of the other aspects described here. An adaptive integration has been developed in our model for handling this problem, combined in some cases with an automatic grid refinement towards the corner (e.g., for wave motion on a slope). They are described in Sections 3.2.2. and 3.3. The effect of the adaptive integration is also extensively checked in Section 6.1. This aspect can be named, in short: *loss of accuracy of the integrals in the corners.*
4. Another numerical aspect comes from the so-called double-node representation of the corners. This method, detailed in Section 4.3, is just *one way* of technically handling the corners by writing two separate equations for each corner, at points with the same coordinates and identical potential, but different normal vectors. For some types of boundary conditions, these equations may simply be identical. If nothing more is done, the problem clearly becomes overdetermined, and the corresponding numerical system matrix poorly conditioned (theoretically singular). The double-node technique requires that this overdetermination is removed by explicitly imposing continuity of the potential at the corner (this is described in Section 4.3.1). The literature is generally not very explicit about this problem and some authors may in fact have skipped this stage and misinterpreted the poor accuracy of the corner solution as to being due to some other reason. This can be named, in short: *continuity conditions for the velocity potential.*
5. Finally, some other relationships between the corner unknowns can always be derived from the boundary conditions (e.g., uniqueness of the velocity vector at the corner). Some of them can be introduced as extra conditions in the corners, and replace one of the corner equations. This is described in Section 4.3.2. In turn, the boundary

conditions on each side of a corner have to be compatible with each other. Otherwise, this will create a singularity of the corner solution. This aspect can be named, in short: *compatibility conditions.*

After analyzing and checking these five aspects of the corner treatment, the optimum relationship between space and time discretizations in the numerical model is also studied from computational results for the propagation of nonlinear water wave in a two-dimensional numerical wavetank. Applications with both exact constant shape waves (solitary waves in Section 6.2) and overturning waves generated by a piston wavemaker (Section 6.3) are presented in detail.

The model equations are briefly recalled in Section 2, the new numerical implementations with the adaptive integration are presented in Section 3 and the corner problems and treatments in Section 4. Generation of wave by a plane piston wavemaker is presented in Section 5. The new improvements of the model are illustrated and checked in Section 6, on simple applications with analytical solutions and also on nonlinear water wave flows in a numerical wavetank. More details about the model equations and the numerical implementation can be found in Grilli, Skourup and Svendsen[13] and Grilli and Svendsen[18]. Preliminary results for the corner treatments have also been reported in Grilli and Svendsen[16] and in Grilli, Svendsen and Otta[19].

2. MATHEMATICAL FORMULATION

2.1. Governing equations

We consider an inviscid irrotational 2-D flow described by a velocity potential $\phi(\mathbf{x}, t)$, and the velocity field is given by $\mathbf{u} = \nabla\phi = (u, w)$. Thus, the continuity equation in the fluid domain $\Omega(t)$ with the boundary $\Gamma(t)$ becomes a Laplace equation for ϕ (Fig. 1),

$$\nabla^2\phi = 0 \quad \text{in } \Omega(t) \tag{1}$$

Using the free space Green's function $G(\mathbf{x}, \mathbf{x}_l) = -\frac{1}{2\pi}\log|\mathbf{x} - \mathbf{x}_l|$, (1) becomes the boundary integral equation (BIE),

$$\alpha(\mathbf{x}_l)\phi(\mathbf{x}_l) = \int_\Gamma \left[\frac{\partial\phi}{\partial n}(\mathbf{x})G(\mathbf{x}, \mathbf{x}_l) - \phi(\mathbf{x})\frac{\partial G(\mathbf{x}, \mathbf{x}_l)}{\partial n}\right] d\Gamma \tag{2}$$

where $\mathbf{x} = (x, z)$ and $\mathbf{x}_l = (x_l, z_l)$ are position vectors for points on the boundary, $\mathbf{n}$ is the unit outward normal vector, and $\alpha(\mathbf{x}_l)$ is a geometric coefficient.

On the free surface $\Gamma_f(t)$, ϕ satisfies the kinematic and dynamic boundary conditions,

$$\frac{D\mathbf{r}}{Dt} = \left(\frac{\partial}{\partial t} + \mathbf{u}\cdot\nabla\right)\mathbf{r} = \mathbf{u} = \nabla\phi \quad \text{on } \Gamma_f(t) \tag{3}$$

$$\frac{D\phi}{Dt} = -gz + \frac{1}{2}|\nabla\phi|^2 - \frac{p_a - p_o}{\rho} \quad \text{on } \Gamma_f(t) \tag{4}$$

with $\mathbf{r}$, the position vector of a free surface fluid particle, g the acceleration due to gravity, z the vertical coordinate (positive upwards and $z = 0$ at the undisturbed free surface), p_a the pressure at the surface, p_o a reference pressure (e.g. at infinity) and ρ the fluid density.

2.2. Boundary conditions

In the applications presented in Section 6, waves are generated by two methods. In the first one, the potential $\phi(x, t_o)$ and the elevation $\eta(x, t_o)$ of a permanent wave solution of (1)-(4) are prescribed at initial time t_o on the free surface $\Gamma_f(t_o)$, and the normal velocity is imposed as u_c over the vertical lateral boundary Γ_{r1},

$$\bar{\phi} = \phi(x, t_o),\ \bar{z} = \eta(x, t_o) \quad \text{on } \Gamma_f(t_o)$$

$$\nabla\phi\cdot\mathbf{n} \equiv \overline{\frac{\partial\phi}{\partial n}} = u_c \quad \text{on } \Gamma_{r1} \tag{5}$$

where the overbar means a specified value. In the second method, waves are generated by simulating a plane wavemaker motion on the boundary $\Gamma_{r1}(t)$. In this case, the motion and normal velocity are specified over the surface of the paddle by,

$$\nabla\phi\cdot\mathbf{n} \equiv \overline{\frac{\partial\phi}{\partial n}} = \mathbf{u}_p(\mathbf{x}_p(t), t)\cdot\mathbf{n} \quad \text{on } \Gamma_{r1}(t) \tag{6}$$

where $(\mathbf{x}_p, \mathbf{u}_p)$ are prescribed wavemaker motion and velocity respectively. Along the stationary bottom Γ_b and the tank extremity Γ_{r2} representing a fixed structure*, we have,

$$\nabla\phi\cdot\mathbf{n} \equiv \overline{\frac{\partial\phi}{\partial n}} = 0 \quad \text{on } \Gamma_b \text{ and } \Gamma_{r2} \tag{7}$$

2.3. Time stepping method

The time stepping, described in detail in Grilli, *et al.*[13], follows the Eulerian-Lagrangian approach used by Dold and Peregrine[5]. It consists of integrating the two nonlinear free surface conditions (3) and (4) at time t, to establish both the new position of the free surface $\Gamma_f(t)$ and the relevant boundary conditions of Laplace's problems at the next step $t + \Delta t$. It uses Taylor expansions in terms of the Lagrangian time derivative (as defined in (3)) and the small time increment Δt, for both the position $\mathbf{r}(t)$ and the potential $\phi(t)$ on the free surface, which corresponds to following in time the pathline of a fluid particle, identical to a node of the discretization used for solving the BIE (2).

All the partial derivatives of ϕ with respect to time satisfy equation (1) so the coefficients of Δt in the Taylor expansions can be found from a sequence $\{\phi, \frac{\partial\phi}{\partial t}, \frac{\partial^2\phi}{\partial t^2}, \dots\}$ of solutions of a succession of Laplace's equations. In a local coordinate system defined by $(\mathbf{s}, \mathbf{n})$, the tangential and normal unit vectors at the free surface, the expansion coefficients are expressed in terms of ϕ, $\frac{\partial\phi}{\partial n}$, $\frac{\partial\phi}{\partial s}$ and $\frac{\partial^2\phi}{\partial s\partial n}$, and of their derivatives along the free surface (see Grilli, *et al.*[13]). The order of these s-derivatives increases like the order m of the Taylor series expansions, and since the derivatives are computed by numerical differentiation, an operation which loses accuracy in the corners of a physical domain, we have so far limited the series and thus the s-derivatives in our model to second order in Δt ($m = 2$). The procedure described can, however, be extended to higher order and, in particular, for space

*Notice, when $\Gamma_{r1}(t)$ or $\Gamma_{r2}(t)$ represent a radiation boundary aimed at absorbing waves propagating in their direction, the potential $\bar{\phi}$ is imposed on these boundaries (this case, we are currently developing, will not be detailed here).

periodic problems where the periodicity conditions can be used to avoid extrapolating the s-derivatives in the corners, higher-order time series have been used by others (see Dold and Peregrine[5] ($m = 3$), Seo[29] ($m = 4$)).

For $m = 2$, the procedure works as follows. After solving a first Laplace problem for $(\phi, \frac{\partial\phi}{\partial n})$ at time t, boundary conditions of a second problem for $(\frac{\partial\phi}{\partial t}, \frac{\partial^2\phi}{\partial t \partial n})$ are determined. Along the free surface, Bernoulli's equation yields,

$$\overline{\frac{\partial\phi}{\partial t}} = -gz - \frac{1}{2}\left|\nabla\phi\right|^2 - \frac{p_a - p_o}{\rho} \quad \text{on } \Gamma_f(t) \tag{8}$$

and along the fixed boundaries, we get,

$$\overline{\frac{\partial^2\phi}{\partial t \partial n}} = 0 \quad \text{on } \Gamma_b \text{ and } \Gamma_{r2} \tag{9}$$

When $\Gamma_{r1}(t)$ represents a plane wavemaker, we have (this boundary condition is detailed in Section 5),

$$\overline{\frac{\partial^2\phi}{\partial t \partial n}} = \left[\frac{d(\mathbf{u}_p \cdot \mathbf{n})}{dt} - \mathbf{u}_p \cdot \nabla(\mathbf{u}_p \cdot \mathbf{n})\right] \quad \text{on } \Gamma_{r1}(t) \tag{10}$$

where $\mathbf{u}_p(\mathbf{x}_p(t), t)$ is, like in (6), the wavemaker velocity as a rigid body, given by the time derivative of the wavemaker motion $\mathbf{x}_p(t)$ following this motion $\frac{d\mathbf{x}_p}{dt}$.

Notice, when $\Gamma_{r1}(t)$ or $\Gamma_{r2}(t)$ represent a radiation boundary, $\frac{\partial\phi}{\partial t}$ is imposed.

3. NUMERICAL IMPLEMENTATION

3.1. Discretization of the Boundary Integral Equation

3.1.1. General

The BIE (2), equivalent to the Laplace's problems (1) for ϕ and $\frac{\partial\phi}{\partial t}$, is solved by a Boundary Element Method (BEM) using a set of N_Γ collocation nodes on the boundary and higher-order elements to interpolate between the collocation nodes. Each integral in (2) is transformed into a sum of integrals over each boundary element.

The technique of shape function representation of the boundary geometry as well as of the variation of the unknowns in the equations (isoparametric elements), has proved to be very efficient in the vast majority of our computations (see Grilli, *et al.*[12,13,14,16], Svendsen and Grilli[30]). This description, however, implies that at the nodes where elements join there is a small discontinuity in the derivatives of the functional description which is not the case at nodes internal to the elements for quadratic and higher-order isoparametric elements. Similar discontinuities and even larger occur at all nodes in linear element approximations.

Using higher-order elements, numerical experiments show that instabilities sometimes occur in the regions of high curvature of the free surface (such as in the jet of a plunging breaker). Since this is found less likely to occur with the less accurate linear elements, we believe these instabilities are due to the generation and (time) propagation of numerical errors resulting from the difference in treatment of the nodes in the interior and at the extremities of the elements, rather than the discontinuities themselves.

The lesser accuracy of the numerical integrations in the BEM for highly curved elements and the loss of accuracy of the numerical integrations that has been observed in the corners (Section 1, 3rd aspect), create additional errors and may add to the importance of these discontinuities.

Quasi-spline elements have been implemented to ensure continuity of the free surface slope (Section 3.1.2.) and improved integrations (Section 3.2.2.) have been developed for removing these losses of accuracy.

3.1.2. Quasi-spline elements

Discontinuities in the slope of the boundary are removed by using quasi-splines elements (see e.g., Longuet-Higgins and Cokelet[24]), which combine a cubic spline approximation of the geometry and a linear shape function model of the fields. These elements are used on the free surface only in combination with the higher-order isoparametric elements on the rest of the boundary. Full cubic spline elements are not used for several reasons: one is, they require knowledge of the gradients of the fields at the free surface extremities; a second is, they have been found computationally time consuming (Seo[29]).

To be able to model breaking waves, the spline approximation of the geometry must account for a multi-valued free surface. For that purpose, the point index τ (also used by Longuet-Higgins and Cokelet) is adopted as a parameter, whose value is equal to the index of the free surface nodes, at the position of these nodes (i.e., 1 to N_f where N_f is the total number of free surface nodes). Instead of defining the splines in polar coordinates, however, regular cartesian coordinates are used to derive two single-valued spline approximations of the free surface: $x = x(\tau)$ and $z = z(\tau)$ (where $\mathbf{r} = (x, z)$ represents a free surface point). Hence, at the free surface nodes,

$$x_j = x(\tau_j);\ z_j = z(\tau_j) \quad j = 1, \ldots, N_f \tag{11}$$

Two regular cubic spline analyses are performed on the free surface for the points (x_j, τ_j) and (z_j, τ_j). In such analyses, the slope has to be specified at the points located at each extremity of the approximated curve. In this case, $\frac{dx}{d\tau}$ and $\frac{dz}{d\tau}$ have to be provided at both extremities of the free surface. They are estimated here, based on cubic polynomials fitted to the 4 first and 4 last nodes of the free surface. In some particular cases, however, the slope at one extremity of the free surface can be deduced from the physics of the problem and imposed explicitly as a boundary condition to the geometry (see Section 4.3.).

All the BEM integrals are computed on a reference element Γ_ξ to which each element on the actual boundary Γ_e^k is related by a change of variable (see Grilli, *et al.*[13], for the transformation in case of isoparametric elements). The reference element for the quasi-splines is a 2-node element of boundary with the intrinsic coordinate $\xi \in [-1, +1]$. The Jacobian of the transformation from the *cartesian* quasi-spline element k, defined on the nodes $(j, j+1)$ of the free surface, to Γ_ξ is,

$$\frac{\partial s_k}{\partial \xi}(\xi) = \frac{\partial s_k}{\partial \tau}(\xi)\,\frac{\partial \tau}{\partial \xi}(\xi) \text{ with } \xi(\tau) = 2(\tau - \tau_j) - 1 \tag{12}$$

where s_k denotes the curvilinear abscissa in the element k. Thus, by definition and by (12),

$$\frac{\partial s_k}{\partial \xi}(\xi) = \frac{1}{2}\left[\left(\frac{dx}{d\tau}(\xi)\right)^2 + \left(\frac{dz}{d\tau}(\xi)\right)^2\right]^{1/2} \tag{13}$$

where the derivatives with respect to τ of x and z are deduced from the sections of the two spline approximations (11) corresponding to the k-th quasi-spline boundary element of the free surface.

3.1.3. Algebraic system of equations

The BIE (2) discretized and expressed for each collocation node l of the boundary, leads to a linear algebraic system of equations for the unknown field u (either ϕ or $\frac{\partial\phi}{\partial t}$). Boundary conditions $\overline{u_s}$ on Γ_d (Dirichlet boundary) and $\overline{\frac{\partial u_p}{\partial n}}$ on Γ_n (Neumann boundary), have been discretized for consistency, the same way as u and $\frac{\partial u}{\partial n}$. Here s refers to nodes on boundary section Γ_d (total N_{Γ_d} nodes) and p refers to nodes on Γ_n (total N_{Γ_n} nodes), and the overbars denote known imposed values. We get the system,

$$[c_{lp} + K_{n_{lp}}]U_p - K_{d_{ls}}\frac{\partial U_s}{\partial n} = K_{d_{lp}}\overline{\frac{\partial U_p}{\partial n}} - [c_{ls} + K_{n_{ls}}]\overline{U}_s \equiv \mathscr{K}_{lj}\mathscr{X}_j = \mathscr{L}_l \qquad (14)$$

where the summation convention of repeated indices is used and, using j for s or p, $\mathscr{K}_{lj}$, $\mathscr{X}_j$ and $\mathscr{L}_l$ represent the system matrix, unknown and load vectors, respectively, with the following definitions,

$$K_{n_{lj}} = \sum_{k=1}^{M+M_f}\int_{\Gamma_\xi} N_j(\xi)\frac{\partial G(\mathbf{x}(\xi),\mathbf{x}_l)}{\partial n}\frac{\partial s_k}{\partial \xi}(\xi)\,d\xi = \sum_{k=1}^{M+M_f} I^k_{n_{lj}}$$

$$K_{d_{lj}} = \sum_{k=1}^{M+M_f}\int_{\Gamma_\xi} N_j(\xi)G(\mathbf{x}(\xi),\mathbf{x}_l)\frac{\partial s_k}{\partial \xi}(\xi)\,d\xi = \sum_{k=1}^{M+M_f} I^k_{d_{lj}}$$

$$l, j = 1,\ldots,N_\Gamma;\ s = 1,\ldots,N_{\Gamma_d};\ p = 1,\ldots,N_{\Gamma_n};$$

$$N_\Gamma = N_{\Gamma_d} + N_{\Gamma_N} \qquad (15)$$

U_j denotes the value of u and $N_j(\xi)$ the reference element shape function, at node j, $\frac{\partial s_k}{\partial \xi}$ is the Jacobian in the k-th element and $M_\Gamma = M + M_f$ is the total number of elements of the discretization (with M_f the number of elements on the free surface). In case of quasi-spline elements, $M_f = (N_f - 1)$, $N_j(\xi)$ is linear and $\frac{\partial s_k}{\partial \xi}$ is computed by (13) in the k-th element.

c_{lj} represents a diagonal matrix whose diagonal coefficients c_{ll} are equivalent to the geometric coefficients $\alpha(\mathbf{x}_l)$ in (2). Instead of computing the c_{ll} by a direct numerical evaluation, these coefficients are deduced by the rigid mode technique (Brebbia[1]) which has been shown to improve the conditioning of the algebraic system (see Grilli, *et al.*[13]).

3.2. Evaluation of the matrix terms

3.2.1. Element by element numerical integration

Due to the higher-order shape functions or splines used in the interpolations, integrals in (15) cannot in general be calculated analytically over each element. When the collocation node l does not belong to the integrated element k, a standard Gauss-Legendre quadrature is used.

When l does belong to the element k, a kernel transformation developed for higher-order elements is applied to the weakly singular $I^k_{d_{lj}}$ which is then integrated by a numerical quadrature, exact for the logarithmic singularity. Though it is not singular, important variations of the integrand occur for $I^k_{n_{lj}}$, when l belongs to an element with high curvature (like in the crest of a wave approaching breaking) which leads to a loss of accuracy of its regular integration. This integration is improved by performing on $I^k_{n_{lj}}$ a change of variable $\mu_l(\xi) = \arctan\frac{z(\xi)-z_l}{x(\xi)-x_l}$ and an analytical integration by parts, before using the numerical quadrature, which both result in the somewhat smoothing out of the large variations of the integrand over the element. Both these cases are detailed in Grilli[11] and Grilli, *et al.*[13].

3.2.2. Adaptive integration

In connection with the 3rd aspect in Section 1, an adaptive numerical integration method is developed and used for improving the accuracy of the regular integrations made with respect to a collocation node $\mathbf{x}_l$, not belonging to the considered element k, from which the element is seen with too large an intercept angle (say $\alpha_l > \alpha_{max}$). This indeed leads to large variations of the integral kernels over the element which cannot be quite caught by regularly spaced Gauss points ($\frac{\partial G}{\partial n}$ being, again, the most sensitive term to this). Large intercept angles α_l occur in the discretization for the elements close to the corners and also when the distance between two boundaries tends to vanish (e.g. through time updating of the fluid domain geometry during wave motion on a slope). In general also large angles occur when the discretization mesh varies quite a lot from one part of the boundary to another one (e.g. due to high ratio length over height of the fluid domain, or due to the concentration of fluid particles-collocation nodes in some region of the flow).

The adaptive integration performs ns binary subdivisions of the element k into segments within which the number of integration points (GP) is kept constant. The subdivision procedure divides the reference element geometry ($\Gamma_\xi \equiv \xi \in [-1, +1]$) into 2^{ns} equal segments of length 2^{1-ns}, until the intercept angle α_{li} of segment i seen from the collocation point $\mathbf{x}_l$ in the actual geometry, becomes smaller than a preset angle α_{max} (i.e. $\alpha_{li} < \alpha_{max}$; $i = 1,\ldots,2^{ns}$). Then, each segment is itself mapped onto the interval $[-1, +1]$. Both types of integral over an element k in (15), say I^k for $I^k_{n_{lj}}$ or $I^k_{d_{lj}}$, can be written as,

$$I^k \equiv \int_{\Gamma_\xi}\mathscr{F}_k(\xi)\,d\xi = \frac{1}{2^{ns}}\sum_{i=1}^{2^{ns}}\int_{-1}^{+1}\mathscr{F}_k(\xi_i(\gamma))\,d\gamma \qquad (16)$$

$$\xi_i(\gamma) = \frac{\gamma}{2^{ns}} + \sum_{b=1}^{ns}\frac{(-1)^{i+B(i,b)}}{2^{ns-b+1}};\quad B(i,b) = \mathrm{INT}\left[\frac{i-1}{2^{ns-b}}\right]$$

where $\mathscr{F}_k(\xi)$ represents the product of G (or $\frac{\partial G}{\partial n}$), a shape function and the Jacobian $\frac{\partial s_k}{\partial \xi}$. Integrals in (16) are computed by a regular Gauss quadrature, with respect to the variable γ. Almost arbitrary accuracy can be achieved in the integrations provided ns is chosen large enough. To reduce the computation time, however, the number of successive binary subdivisions is limited to $ns = 4$ in the applications (i.e. 16 segments), and $\alpha_{max} = 40°$ is selected, based on our computing experience. Notice, for $ns = 0$, the integration formula (16) reduces to one segment of length 2, which corresponds to the usual regular integral over Γ_ξ.

The adaptive integration (16) is computationally quite efficient over one element, for a given ns, with respect to a given $\mathbf{x}_l$. The selection of the number of subdivisions ns for all the elements k, with respect to all the N_Γ colloca-

tion points l, however, is computationally expensive. It requires $(2^{n_s})!$ computations of angles α_{ij} for each couple of values (k, l) (to be compared with the maximum), which themselves require to perform the change of variable from the reference element Γ_ξ to the actual geometry Γ_e^k.

It is therefore necessary to *a priori* restrict these operations to a number of pairs (k, l) in the computation data. In general, the 8 elements defining the 4 domain corners are selected, and also the elements on parts of the boundary discretization which, one anticipates, will become close to each other in the following time steps (e.g. tip of a plunging breaker, wave running down on a slope, ...). These selections can be and are, of course, interactively modified during the computations when the domain geometry changes through the time evolution. Doing so, the extra computational effort of performing adaptive integrations is, in general, reduced to a few percent of the computation time per time step, used otherwise without them.

3.3. *Automatic grid refinement on a slope*

It is observed that, during wave motion on a slope (runup-rundown), the size of the last element on the free surface may become much smaller than the size of the first neighbouring element on the slope. This leads to somewhat less accurate integrations close to the surface corner, even with the adaptive integration procedure. To improve the accuracy of the integrations, the discretization on the slope is stretched, as suggested by Klopman[20], according to an exponential law which imposes the length of the upper element on the wall (closest to the free surface) to be the same at all time steps as the length of the last element on the free surface. The other elements on the wall are, accordingly, becoming wider towards the bottom. This automatic grid refinement, associated with the adaptive integration, increase the accuracy of the numerical solution in the corner by several orders of magnitude.

4. FREE SURFACE INTERSECTION WITH MOVING BODIES

4.1. *Mathematical problem*

When waves are generated by simulating a wavemaker or a body motion, there is a corner on the boundary curve, where body and free surface meet. The same situation is also created at the intersection with other surface piercing structures, like fixed slopes. The *possible mathematical singularity of the solution* will be analyzed here (1st aspect, Section 1).

The flow near the intersections between a free surface and a moving solid body has given rise to substantial concern in the literature since Kravtchenko[21] showed that for linear waves and harmonic motion, the intersection with a moving vertical wall would generally create an incompatibility between the flow requirements of the boundary conditions along the free surface and the wall. Kravtchenko's derivations indicated a weak logarithmic singularity of the complex potential $W \sim z^2 \log z$, with $z = x + iy$. This corresponds to a bounded free surface elevation at the intersection, but the second and higher derivatives of W are singular.

For the case of an impulsively accelerated wall (i.e., with theoretically infinite initial acceleration) Peregrine[26] (and Lin[22] using a different approach) found a stronger singularity of the complex potential $W \sim z \log z$, which corresponds to an unbounded free surface at the intersection (varying as $\log x$). This seemed to be confirmed by the experiments by Greenhow and Lin[9].

In a more detailed investigation, Roberts[27] found that if the acceleration $\dot{u}_p = \frac{d^2 x_p}{dt^2}$ of the vertical wall remains bounded, the amplitude of the free surface at the wall will also be bounded, although not particularly smoothly behaved (short dispersive waves appear close to the intersection). Roberts finds that, with a quasi-impulsive start over a small but finite time, gravity cannot be neglected, as in Peregrine's analysis, and waves of large wavenumber (short waves) cannot be neglected, as in Lin's. In particular, if the initial paddle acceleration is $\dot{u}_p \sim t^{p-1}$ with $p > 1$, the acceleration is bounded at small times and *gravity is dominant*. Hence, the problem can be linearized and the singularity of W reduces to $z^2 \log z$ with a bounded free surface elevation at the intersection (this defines a *weakly-nonlinear* regime). He also finds that, even though the amplitude at the wall remains finite, away from the wall the free surface variation *is* logarithmic to leading order as, e.g., computed by Lin, Newman and Yue[23] and verified by Greenhow and Lin's experiments (even the dramatic acceleration they produced by a seldge hammer is still not mathematically an impulsive start). Notice that Roberts' analysis also showed a well-behaved solution in the case of an acceleration exponentially increasing with time.

Cointe[2,3], following a procedure similar to Kravtchenko's, confirmed the results by Roberts and extended them to a non-vertical wavemaker. With the angle between the paddle and the undisturbed freed surface denoted by Θ, Cointe finds, the higher singularity of the complex potential is $\sim z^{\pi/\Theta}$ (i.e., of an order similar to the singularity at a Neumann–Neumann corner in a Laplace problem), for $\Theta \in]0, \pi[$, and $\frac{\pi}{\Theta}$ not an integer (for integer ratios, logarithmic singularities have to be introduced). For the case $\Theta = \frac{\pi}{2}$, he explicitly derives,

$$W(z) = \phi + i\psi \sim A(t) + [u_p + i\beta(t)]z + \frac{1}{\pi}\ddot{u}_p z^2 \log z + \ldots \tag{17}$$

where $x_p(t)$, $u_p(t)$, $\dot{u}_p(t)$ are the position, horizontal velocity and acceleration of the paddle motion, and $A(t)$ and $\beta(t)$ are complex and real functions of time, respectively. Thus, in (17), the order of the singularity agrees with the results by both Kravtchenko[21] and Roberts[27] (Cointe shows, (17) can even be explicitly derived from Roberts results).

Cointe, *et al.*[4], also investigated the case of an impulsive vertical paddle motion, with velocity following a step function at $t = 0$. Gravity can be neglected in this case (as in Peregrine[26]), and the problem is devided into an exterior problem whose (linearized) solution, given by Peregrine[26] and Lin[22], is singular with $W \sim z \log z$, and an interior nonlinear problem which gives the behavior of the solution at the intersection. The interior solution is expressed by self-similarity in case of large depth and matched to the exterior solution. Cointe, *et al.*, however, were unable to provide any result (even linearized) or

conclusion about this interior solution (except in the case where the paddle is pulled).

Following the general conclusions by Cointe[3], the existence of a strong singularity at the corner for the fully nonlinear case with *large* or unbounded initial acceleration of the paddle is suspected but has still to be proved theoretically. The linearized exterior solution corresponding to this case, however, is proved to be singular with $W \sim z \log z$ and, hence, an unbounded free surface and numerical problems at the corner can be expected. When the initial acceleration is *bounded* ($p > 1$ in Roberts' power law) and small enough with respect to gravity, the initial flow belongs to a *weakly-nonlinear* regime, with a weak singularity of the free surface potential at the intersection ($W \sim z^2 \log z$) and a finite free surface elevation. This can be expected not to pose any numerical problems provided proper numerical treatment of the corner is done (see Section 4.3.). In our model, indeed, no singular behavior or instability of the solution is observed, provided the acceleration remains small during the first few time steps starting the computations.

4.2. Numerical problem

Care must be taken to ensure the well-posedness of the flow equations and boundary conditions to be solved by the numerical method. It follows from the outline in Section 4.1. that one has to account for the fact that both the potential and its normal gradient are known on the body part of the corner, whereas there is a different and *a priori* unknown normal gradient on its free surface part.

Lin[22] and Lin, Newman and Yue[23] handled this problem by specifying both the potential ϕ and the stream function ψ at the body part of the corner in their complex Cauchy integral theorem formulation. Doing so, they could generate nonlinear waves by a wavemaker. Using a similar technique, Greenhow and Lin[8] simulated nonlinear wedge entries in water. Dommermuth and Yue[6], following the same principle as Lin, *et al.*, imposed both the potential and its normal derivative at the body part of the corner in their BEM formulation. A similar numerical treatment of the corners has been implemented in our model and described in the following Section.

Cointe[3] introduced two numerical treatments of the corner. In the weakly nonlinear regime (with small initial acceleration), he uses his explicit solution (17) of the flow (which actually constitutes a *removal of the corner singularity* in the sense of the 2nd aspect in Section 1), whereas in the fully nonlinear case, he simply determines the corner value of the normal gradient on both sides by linear extrapolation from its value in the previous element on the boundary. This, Cointe believes, is equivalent to the "regularity conditions" introduced by Lin[22] and, consequently, should also be equivalent to our method.

4.3. Continuity and compatibility conditions

Double (collocation) nodes are used at the corners A to D (Fig. 1) to provide two different normal directions and unknowns on the two sides of each corner and *continuity* of ϕ (or $\frac{\partial\phi}{\partial t}$) at the two nodes is explicitly imposed in the BEM algebraic system (4th aspect, Section 1).

In some cases, extra relations (kinematic or geometric) between the ϕ's and the $\frac{\partial\phi}{\partial n}$'s (or $\frac{\partial\phi}{\partial t}$'s and $\frac{\partial^2\phi}{\partial t\partial n}$s') exist at the corner points (the *compatibility conditions*). Though they should automatically be satisfied by the numerical solution, they are not exactly fulfilled due to numerical errors. Since there is no damping in the model, these small errors can add up through time updating which sometimes leads to instability of the solution. Therefore, the errors are reduced by explicitly imposing these extra relations to the solution after each time step (5th aspect, Section 1).

4.3.1. Double-nodes and potential continuity

For double-nodes, the coordinates of both nodes are the same but the normal vectors differ and, therefore, $\frac{\partial\phi}{\partial n}$ and $\frac{\partial^2\phi}{\partial t\partial n}$ are different. Also the type of boundary condition may be different at the two nodes. Two expressions of the BIE (2) are derived at each corner double-node, for which continuity of ϕ (and $\frac{\partial\phi}{\partial t}$) is explicitly imposed in the algebraic system (14) of system matrix $\mathcal{H}_{ij}$ and load vector $\mathcal{L}_i$. Only the case of the boundary value problem for (ϕ, $\frac{\partial\phi}{\partial n}$) is described here. The procedure, however, is identical for ($\frac{\partial\phi}{\partial t}$, $\frac{\partial^2\phi}{\partial t\partial n}$).

- *Dirichlet-Neumann*: In the case of wave generation by a wavemaker or by a potential on the free surface, the value of the potential is imposed at the free surface corners A and B, say at node s, as ϕ_s (Dirichlet condition) and the normal velocity on the lateral boundaries, say at node p, as $\frac{\partial\phi_p}{\partial n}$ (Neumann condition, different or equal to zero for a moving or fixed body). Two equations are obtained for s and p, in the algebraic system (14). At node p, however, by continuity at the double-node, the potential is the same as in s: $\phi_p = \overline{\phi_s}$, and no actual unknown is left. Instead of removing the equation p from the system and reducing its size by one (which may be computationally expensive), the algebraic system is modified at line p, to exactly satisfy the continuity condition,

$$\mathcal{H}_{pj} = 0, \forall j \neq p \text{ and } \mathcal{H}_{pp} = \mathcal{M}, \mathcal{L}_p = \mathcal{M}\overline{\phi_s},$$
$$\mathcal{M} = |\mathcal{H}_{ii}|^{max} \tag{18}$$

  where the weighting by the maximum diagonal element $\mathcal{M}$ ensures a good conditioning of the modified system. The solution of (14) modified by (18) automatically satisfies the continuity of the potential at the double-node.
- *Neumann-Neumann*: In the case of wave generation by a wavemaker or by a potential imposed on the free surface, the normal velocity is specified on both sides of the corners at the bottom double-nodes C and D, say at node q, as $\frac{\partial\Phi_q}{\partial n} = 0$ on the bottom and at node p, as $\frac{\partial\Phi_p}{\partial n}$ on the lateral boundary (different or equal to zero for a moving or fixed body). Two equations are obtained for p and q in the algebraic system (14), each of them for the (same) unknown potential at the corner. Hence, the system matrix $\mathcal{H}_{ij}$ is singular. To make it solvable, one of the equations, say at node q, is modified on a way similar to above, to explicitly satisfy the continuity condition $\phi_q = \phi_p$,

$$\mathcal{H}_{qj} = 0, \forall j \neq p, q \text{ and } \mathcal{H}_{qq} = \mathcal{M},$$
$$\mathcal{H}_{qp} = -\mathcal{M}, \mathcal{L}_q = 0 \tag{19}$$

- *Dirichlet-Dirichlet*: When a radiation condition is imposed on a lateral boundary, potential is specified identical on both sides of a free surface corner A or B, say at nodes s and p, as $\overline{\phi_s} = \overline{\phi_p}$ (Dirichlet conditions). Due to the 2 different normal directions on the two corner sides, the (unknown) $\frac{\partial\phi}{\partial n}$'s are to be found different, say $(\frac{\partial\phi_s}{\partial n}, \frac{\partial\phi_p}{\partial n})$, which corresponds to having 2 different equations at lines s and p of the system (14). Hence, the system matrix $\mathscr{K}_{ij}$ is non-singular and no continuity condition is required in this case.

As expected (Section 1), it is observed in the applications, that by introducing the *continuity* conditions (18), (19) at the double-nodes, the condition number of the system matrix $\mathscr{K}_{ij}$ is significantly reduced and the accuracy of the solution is thereby dramatically improved, in particular, close to the corner nodes.

4.3.2. Compatibility conditions

Again, only the case of $(\frac{\partial\phi}{\partial s}, \frac{\partial\phi}{\partial n})$ is discussed. However, all the equations in the following are identically valid and used also for $(\frac{\partial^2\phi}{\partial t\partial s}, \frac{\partial^2\phi}{\partial t\partial n})$.

1. *Kinematic conditions*:

- *Dirichlet-Dirichlet*: When the potential is known on one part of the boundary, the tangential velocity $\frac{\overline{\partial\phi}}{\partial s}$ is known as well, within the accuracy of the interpolation procedure used for computing it*. When the potential and, hence, $\frac{\overline{\partial\phi}}{\partial s}$ are imposed on both sides of a free surface corner, say at nodes p and q, the (unique) corner velocity vector $(u, w) = \mathbf{u}_p = \mathbf{u}_q$ can be expressed at both nodes as a function of their own normal and tangential velocities, i.e. $(\frac{\partial\phi_p}{\partial n}, \frac{\overline{\partial\phi_p}}{\partial s})$ and $(\frac{\partial\phi_q}{\partial n}, \frac{\overline{\partial\phi_q}}{\partial s})$ by,

$$\begin{aligned} u &= \frac{\overline{\partial\phi_p}}{\partial s}\cos\beta_p - \frac{\partial\phi_p}{\partial n}\sin\beta_p \\ &= \frac{\overline{\partial\phi_q}}{\partial s}\cos\beta_q - \frac{\partial\phi_q}{\partial n}\sin\beta_q \\ w &= \frac{\overline{\partial\phi_p}}{\partial s}\sin\beta_p + \frac{\partial\phi_p}{\partial n}\cos\beta_p \\ &= \frac{\overline{\partial\phi_q}}{\partial s}\sin\beta_q + \frac{\partial\phi_q}{\partial n}\cos\beta_q \end{aligned} \tag{20}$$

or, by reordering the knowns and unknowns,

$$\begin{aligned} &\frac{\partial\phi_p}{\partial n}\sin\beta_p - \frac{\partial\phi_q}{\partial n}\sin\beta_q = \\ &\left[\frac{\overline{\partial\phi_p}}{\partial s}\cos\beta_p - \frac{\overline{\partial\phi_q}}{\partial s}\cos\beta_q\right] = u' \\ &\frac{\partial\phi_q}{\partial n}\cos\beta_q - \frac{\partial\phi_p}{\partial n}\cos\beta_p = \\ &\left[\frac{\overline{\partial\phi_p}}{\partial s}\sin\beta_p - \frac{\overline{\partial\phi_q}}{\partial s}\sin\beta_q\right] = w' \end{aligned} \tag{21}$$

*Our computations of the s-derivatives use a sliding 4th-order polynomial (Grilli, *et al.*[13]). Hence, they are getting less accurate in the corners because they are based more on an extrapolation than an interpolation. Another method for calculating $\frac{\partial\phi}{\partial s}$ in the corners would be to using hypersingular equations (see Gray[16]). That method may be more accurate since it would be based on integration rather than differentiation.

where $\mathbf{s} = (\cos\beta, \sin\beta)$ is the tangential vector (positive clockwise along the boundary), and the expressions noted (u', w') are only functions of the geometry and boundary conditions. Hence, the unknown $\frac{\partial\phi}{\partial n}$'s at the double-nodes can directly be obtained by solving (21), which could simply be done by replacing the lines p and q of the algebraic system (14), by the two equations (21). It has been found, however, by making some numerical experiments, that the solution is more accurate when only one of the equations (21) (the relation for the lateral boundary q) is introduced in the algebraic system, as a compatibility condition. This, we believe, is due to the loss of accuracy of the s-derivatives in the corner, mentioned above. The other equation, for $\frac{\partial\phi_p}{\partial n}$, is the BIE (2) whose algebraic expression is at line p of the system. Thus, line q of $\mathscr{K}_{ij}$ becomes,

$$\begin{aligned} &\mathscr{K}_{qj} = 0, \forall j \neq p, q \text{ and } \mathscr{K}_{qq} = \mathscr{M}\cos\beta_q, \\ &\mathscr{K}_{qp} = -\mathscr{M}\cos\beta_p, \mathscr{L}_q = \mathscr{M}\, w' \end{aligned} \tag{22}$$

- *Dirichlet-Neumann*: After solution of the system (14), modified by (18), the $\frac{\partial\phi}{\partial s}$ have to be calculated at the free surface, to be used in the time updating. This is normally done in the model by numerical interpolation (as mentioned above). At the free surface double nodes, however, equations (20) are still valid, now, with $\frac{\partial\phi_q}{\partial n}$ being known from the lateral boundary condition (Neumann condition), and $\frac{\widetilde{\partial\phi_p}}{\partial n}$ being known at the free surface from the BEM solution (Dirichlet condition; the tilde refers to a value whose approximate numerical solution only is known). Equations (20) can therefore be used for computing $\frac{\partial\phi}{\partial s}$'s which explicitly satisfy uniqueness of the velocity vector at the double-nodes $(u, w) = \mathbf{u}_p = \mathbf{u}_q$. We get,

$$\begin{aligned} &\frac{\partial\phi_p}{\partial s}\cos\beta_p - \frac{\partial\phi_q}{\partial s}\cos\beta_q = \\ &\left[\frac{\widetilde{\partial\phi_p}}{\partial n}\sin\beta_p - \frac{\overline{\partial\phi_q}}{\partial n}\sin\beta_q\right] = u' \\ &\frac{\partial\phi_p}{\partial s}\sin\beta_p - \frac{\partial\phi_q}{\partial s}\sin\beta_q = \\ &\left[\frac{\overline{\partial\phi_q}}{\partial n}\cos\beta_q - \frac{\widetilde{\partial\phi_p}}{\partial n}\cos\beta_p\right] = w' \end{aligned} \tag{23}$$

which is then solved for the $\frac{\partial\phi}{\partial s}$'s as,

$$\begin{aligned} \frac{\partial\phi_p}{\partial s} &= \frac{w'\cos\beta_q - u'\sin\beta_q}{\sin(\beta_p - \beta_q)} \\ \frac{\partial\phi_q}{\partial s} &= \frac{w'\cos\beta_p - u'\sin\beta_p}{\sin(\beta_p - \beta_q)} \end{aligned} \tag{24}$$

Only the tangential velocity on the free surface $\frac{\partial\phi_p}{\partial s}$ is needed in the time updating. From (24) we get,

$$\frac{\partial\phi_p}{\partial s} = \frac{\overline{\partial\phi_q}}{\partial n}\csc(\beta_p - \beta_q) - \frac{\widetilde{\partial\phi_p}}{\partial n}\cot(\beta_p - \beta_q) \tag{25}$$

In the particular case of a plane Neumann boundary Γ_{r1} of angle θ with respect to the bottom (as in wave

generation by a wavemaker), $\beta_q = \theta$. For a *piston wavemaker*, $\theta = \frac{\pi}{2}$, thus $\cos\beta_q = 0$, $\sin\beta_q = 1$ and, by (25),

$$\frac{\partial\phi_p}{\partial s} = \widetilde{\frac{\partial\phi_p}{\partial n}}\tan\beta_p - \overline{\frac{\partial\phi_p}{\partial n}}\sec\beta_p \tag{26}$$

In case of a plane *flap wavemaker* oscillating at an angle $\theta(t)$ with respect to the bottom, we get the full expression (25) with $\beta_q = \theta(t)$.
Finally, in case of a plane impermeable slope Γ_{r2}, of angle θ with respect to the bottom (Fig. 1), $\beta_q = \theta - \pi$, hence $\cos\beta_q = -\cos\theta$, $\sin\beta_q = -\sin\theta$, and $\frac{\partial\phi_q}{\partial n} = 0$. Thus by (25),

$$\frac{\partial\phi_p}{\partial s} = \widetilde{\frac{\partial\phi_p}{\partial n}}\cot(\theta - \beta_p) \tag{27}$$

which simply expresses that the velocity vector is unique and parallel to the slope.

2. *Geometric conditions*:
In some Dirichlet–Neumann cases, the slope of the free surface at a double-node can directly be deduced from the physics of the problem, and used as an improved boundary condition for the spline approximation of the free surface (see Section 3.1.2.).

- *Fixed body*: The free surface slope $\frac{dz}{dx}$ is zero by symmetry, for a fixed vertical Neumann boundary Γ_{r1} (vertical wall). Hence, with the point index representation, we get: $\frac{dz}{dt} = 0$.
The free surface slope is limited to avoid unrealistic intersection with a plane boundary Γ_{r2} of angle θ (which otherwise may unwantingly happen, e.g., during wave rundown) to: $\arctan\frac{dz}{dx} \le \theta$ or $\frac{dz}{dx} \le \frac{dz}{dr}\tan\theta$.
- *Moving body*: The free surface slope is artificially limited for a moving vertical Neumann boundary $\Gamma_{r1}(t)$ (piston wavemaker), to avoid unrealistic intersection with the wavemaker (e.g., in case of large acceleration) to: $|\arctan\frac{dz}{dx}| \le \frac{\pi}{2}$ or $\frac{dx}{dt} \ge 0$.
Finally, for a moving plane Neumann boundary $\Gamma_{r1}(t)$ of angle θ (flap wavemaker), we similarly get: $\frac{dz}{dt} \ge \frac{dz}{dt}\tan\theta$.

It is observed in the applications, that the introduction of the *compatibility* conditions (22), (25)–(27) at the double-nodes significantly reduces the local numerical errors during time updating and, consequently, the instabilities of the solution which otherwise may show up (e.g. in higher-order terms like $\frac{\partial^2\phi}{\partial t\partial n}$, $\frac{\partial^2\phi}{\partial s^2}$) and propagate.

5. WAVE GENERATION BY A PLANE WAVEMAKER

5.1. General boundary condition

A plane wavemaker motion $\mathbf{x}_p(t)$ of velocity $\mathbf{u}_p(\mathbf{x}_p(t), t)$ is prescribed on the boundary $\Gamma_{r1}(t)$, to which it corresponds the boundary conditions (6) and (10), for $\frac{\partial\phi}{\partial n}$ and $\frac{\partial^2\phi}{\partial t\partial n}$. The equation for $\frac{\partial^2\phi}{\partial t\partial n}$, however, includes a time derivative with respect to the rigid body motion that needs to be developed with great care. This has been done by Cointe[3] for a general rigid body motion with translation α, and rotation θ at $\mathbf{x}_g$. In case of a plane rigid body, Cointe's expression reads,

$$\frac{\partial^2\phi}{\partial t\partial n} = (\ddot{\alpha}\cdot\mathbf{n}) + \dot{\theta}\left[(\dot{\alpha}\cdot\mathbf{s}) - \frac{\partial\phi}{\partial s}\right] - \frac{\partial^2\phi}{\partial n\partial s}(\dot{\alpha}\cdot\mathbf{s}) + \frac{\partial^2\phi}{\partial s^2}(\dot{\alpha}\cdot\mathbf{n}) \tag{28}$$

where the dots denote absolute time derivatives with respect to the body motion ($\frac{d}{dt}$ like in (10)).

The motion and boundary conditions are expressed for a *piston wavemaker*, which will be the only one used in the following applications (similar derivations are reported in Grilli and Svendsen[17], for the generation of periodic waves by a *flap wavemaker*). This represents a flat vertical plate moving with horizontal motion $x_p(t)$ and velocity $u_p(x_p(t), t) = \dot{x}_p(t)$, corresponding to the wave motion to be generated. We have,

$$\mathbf{n} = (-1, 0),\ \mathbf{s} = (0, 1),\ \dot{\theta} = \ddot{\theta} = 0$$
$$\alpha = \mathbf{x}_p = (x_p, 0),\ \dot{\alpha} = \mathbf{u}_p = (u_p, 0),\ \ddot{\alpha} = \dot{\mathbf{u}}_p = (\dot{u}_p, 0) \tag{29}$$

Hence, from (6),(28), the boundary conditions read,

$$\frac{\partial\phi}{\partial n} = -u_p,\ \frac{\partial^2\phi}{\partial t\partial n} = -\dot{u}_p - u_p\frac{\partial^2\phi}{\partial s^2} \tag{30}$$

5.2. Generation of a first-order solitary wave by a piston wavemaker

In the following, primes denote dimensionless variables: lengths are non-dimensionalized by d, times by $\sqrt{\frac{d}{g}}$, velocities by $\sqrt{gd}$ and accelerations by g.

For a wave of permanent form (solitary wave) Goring[7] determined the motion required by a piston wavemaker to generate a specified water surface elevation η immediately in front of the wavemaker (see Grilli & Svendsen[18], for detail) as,

$$x_p(t) = \int_0^t \frac{c\eta}{d+\eta}\,d\tau \tag{31}$$

A *first-order* solitary wave profile of amplitude H' is generated in water of constant depth $d' = 1$,

$$\eta'(x', t') = H'\mathrm{sech}^2[\kappa(x' - c't')] \tag{32}$$

where $\kappa = \frac{\sqrt{3H'}}{2}$ and the celerity $c' = \sqrt{1 + H'}$. Substituting (32) into (31) with $x' = x'_p(t)$ required throughout the integration gives the piston motion. However, since a solitary wave profile extends to infinity in both directions, it has to be truncated at some distance from the origin, before being used in the model. Goring introduced the significant horizontal extension $2\lambda'$ of the wave, corresponding to a reduction in amplitude of the profile to $\eta' = \varepsilon_z H'$. One gets,

$$\lambda' = \frac{l}{\kappa} \text{ with } l = \mathrm{arcosh}[\varepsilon_z^{-1/2}] \tag{33}$$

In the applications (Section 6) we use $\varepsilon_z = 0.002$, i.e. $l \simeq 3.80$.

Hence, wave generation by the wavemaker now starts

at $t'_o = 0$ for $x' = \lambda'$ in the wave profile. Setting $x' = x'_p + \lambda'$ in (32) and integrating (31) we get,

$$x'_p(t') = \frac{H'}{\kappa}\left[\tanh\chi(t') + \tanh\kappa\lambda'\right]$$

$$\chi(t') = \kappa(c't' - x'_p(t') - \lambda') \tag{34}$$

This equation, implicit in x'_p, is solved by Newton iterations for any given t'. Then, $u'_p(t')$ is computed by (31), for $\eta'(x'_p(t'), t')$, and $\dot{u}'_p(t')$ is found by the time derivation of it, following the piston motion. We get,

$$u'_p(t') = H'(1 + H')^{1/2}\frac{1}{\cosh^2\chi(t') + H'}$$

$$\dot{u}'_p(t') = \sqrt{3}\,H'^{3/2}(1 + H')\frac{\cosh^3\chi(t')\sinh\chi(t')}{(\cosh^2\chi(t') + H')^3} \tag{35}$$

which, introduced into (30), defines the boundary conditions on the wavemaker.

The initial wavemaker velocity and acceleration at $t'_o = 0$ are deduced as a function of H' and ε_z, by introducing (33), (34) (with $\chi(t'_o) = l$) into (35), as,

$$u'_p(t'_o) = H'(1 + H')^{1/2}\frac{\varepsilon_z}{1 + \varepsilon_z H'}$$

$$\dot{u}'_p(t'_o) = \sqrt{3}\,H'^{3/2}(1 + H')\varepsilon_z\frac{(1 - \varepsilon_z)^{1/2}}{(1 + \varepsilon_z H')^2} \tag{36}$$

which both are approximately proportional to ε_z, for a given H'. Therefore, the initial piston acceleration is controlled by selecting the truncation ε_z of the solitary wave. For $\varepsilon_z = 0.002$ and $H' = 0.5$, for instance, we get $u_p(t_o) \simeq 0.00122\sqrt{gd}$ and $\dot{u}_p(t_o) \simeq 0.00184g$ which is quite small.

6. APPLICATIONS

6.1. Check of accuracy of the corner treatments

Two simple problems with known analytical solution are solved in various geometries and discretizations, to illustrate and check the effects on the accuracy of the numerical solution of the new corner treatments, namely the continuity and compatibility conditions in the corners, and the adaptive integration. Figure 2 shows the sketch and boundary conditions for the first problem (1) with rectangular domain of length $L = 10$ and depth d. The free surface (Dirichlet) and bottom (Neumann) boundary conditions are similar to those of a wave problem with the wave being generated by a potential on the free surface. The lateral boundary conditions are identical to those of a wave radiation problem, with Dirichlet conditions on both lateral boundaries: $\varphi = 0$ and φ_o respectively (as also shown in the Figure; notice $\phi \equiv \varphi$). The second problem (2) is defined the same way, with Neumann boundary conditions instead on both lateral boundaries: $\varphi_n = -1$ and 1 respectively, like in a wavemaker problem with reflection at the other end of the domain. For both problems, the analytical solution is $\varphi = x$ over the domain, and $\varphi_n = 0$ on the free surface and on the bottom, and -1 and 1 on the left and right lateral boundaries, respectively.

These two problems are solved using the wave propagation model, in domains with different aspect ratios $\frac{L}{d}$ (Tables 1, 2, and 3), with accordingly varying horizontal (Δx) and vertical (Δz) grid steps (distance on the boundary between two successive nodes), and total discretizations of N_Γ nodes with M_Γ linear 2-node elements*. The computation time varies between 0.07s and 2.90s CPU (IBM 3090/300) for all the cases in Tables 1, 2 and 3 (which corresponds to the solution of 2 Laplace problems, with time updating of the geometry in between).

The maximum error of the numerical solution is quantified, in each case, as the maximum normal gradi-

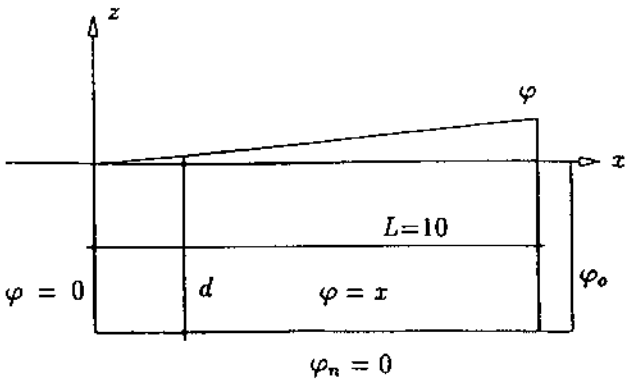

Fig. 2. Sketch of a simple rectangular domain problem with analytical solution, for check on corner treatments and adaptive integration. Length is L = 10 and depth d, with $\frac{L}{d}$ and the discretization like in Tables 1, 2, and 3, and boundary conditions shown for problem 1 only, with φ_o = 10. Notice in problem 2, Neumann conditions $\varphi_n = \mp 1$ are used instead on the lateral boundaries.

Table 1. Maximum error of normal gradient on the free surface as a function of the number of Gauss points (GP) per element: Results are either with adaptive integration in the corner elements ($|\varphi_n|^{max}_{\Gamma 1,2}$) or without adaptive integration ($|\varphi_n|^{max}_{\Gamma 1,2}$). Subscripts 1 and 2 refer to problems with lateral Dirichlet and Neumann boundary conditions, respectively. The aspect ratio is $\frac{L}{d} = 1$, with $\frac{\Delta x}{\Delta z} = 1$ and the discretization has $N_\Gamma = 24$ nodes and $M_\Gamma = 20$ elements.

	2GP	4GP	6GP	8GP	10GP
$\|\varphi_n\|^{max}_{\Gamma 1}$	$6.3\,10^{-4}$	$3.7\,10^{-6}$	$4.6\,10^{-9}$	$1.4\,10^{-11}$	$3.3\,10^{-14}$
$\|\varphi_n\|^{max}_{a1}$	$8.7\,10^{-5}$	$5.7\,10^{-8}$	$2.5\,10^{-11}$	$2.5\,10^{-14}$	$5.5\,10^{-15}$
$\|\|\varphi_n\|^{max}_{\Gamma 2}$	$1.8\,10^{-3}$	$4.5\,10^{-6}$	$1.4\,10^{-8}$	$1.3\,10^{-11}$	$1.0\,10^{-13}$
$\|\varphi_n\|^{max}_{a2}$	$2.9\,10^{-4}$	$2.2\,10^{-7}$	$4.0\,10^{-11}$	$5.2\,10^{-14}$	$1.2\,10^{-14}$

Table 2. Maximum error of normal gradient on the free surface as a function of grid step $\frac{\Delta x}{d}$. Results are defined as in Table 1. The aspect ratio is $\frac{L}{d} = 1$, $\frac{\Delta x}{\Delta z} = 1$ and the discretization has N_Γ nodes and M_Γ 2-node elements.

$\frac{\Delta x}{d}$	N_Γ	M_Γ	$\|\varphi_n\|^{max}_{\Gamma 1}$	$\|\varphi_n\|^{max}_{a1}$	$\|\varphi_n\|^{max}_{\Gamma 2}$	$\|\varphi_n\|^{max}_{a2}$
0.25	20	16	$2.9\,10^{-14}$	$4.8\,10^{-15}$	$1.1\,10^{-13}$	$1.8\,10^{-14}$
0.20	24	20	$3.3\,10^{-14}$	$5.5\,10^{-15}$	$1.0\,10^{-13}$	$1.2\,10^{-14}$
0.10	44	40	$4.3\,10^{-14}$	$3.7\,10^{-14}$	$1.2\,10^{-13}$	$2.4\,10^{-14}$
0.05	84	80	$1.2\,10^{-13}$	$1.1\,10^{-13}$	$2.8\,10^{-13}$	$8.2\,10^{-14}$
0.025	164	160	$3.3\,10^{-13}$	$4.1\,10^{-13}$	$2.9\,10^{-12}$	$2.3\,10^{-12}$

*Notice since in this case the exact solution is linear, there is no need for using higher-order elements. In wave problems, however, we do use higher-order elements on all boundaries (Sections 6.2, 6.3).

Table 3. Maximum error of normal gradient on the free surface as a function of $\frac{h}{d}$ and $\frac{\Delta z}{\Delta x}$. Results are defined as in Table 1. Notice, $\alpha^{max} = \arctan[1/\frac{\Delta z}{\Delta x}]$ represents the maximum angle of intercept of the free surface and bottom corner elements.

$\frac{h}{d}$	$\frac{\Delta x}{d}$	$\frac{\Delta z}{\Delta x}$	N_Γ	M_Γ	α^{max}	$\lvert\varphi_n\rvert_{r1}^{max}$	$\lvert\varphi_n\rvert_{a1}^{max}$	$\lvert\varphi_n\rvert_{r2}^{max}$	$\lvert\varphi_n\rvert_{a2}^{max}$
1	0.2	1.0	24	20	45°	$3.3\ 10^{-14}$	$5.5\ 10^{-15}$	$1.0\ 10^{-13}$	$1.2\ 10^{-14}$
2	0.4	0.5	24	20	63°	$8.6\ 10^{-11}$	$1.2\ 10^{-14}$	$1.1\ 10^{-10}$	$4.4\ 10^{-15}$
5	0.25	0.8	54	50	51°	$3.1\ 10^{-13}$	$2.4\ 10^{-14}$	$1.4\ 10^{-12}$	$1.3\ 10^{-13}$
10	0.25	1.0	92	88	45°	$1.7\ 10^{-13}$	$2.0\ 10^{-13}$	$1.8\ 10^{-12}$	$1.7\ 10^{-12}$
10	0.25	0.5	100	96	63°	$8.6\ 10^{-11}$	$2.7\ 10^{-13}$	$1.2\ 10^{-10}$	$2.4\ 10^{-12}$
10	0.25	0.25	116	112	76°	$8.4\ 10^{-10}$	$3.6\ 10^{-13}$	$3.9\ 10^{-8}$	$2.2\ 10^{-12}$
10	0.25	0.20	124	120	79°	$1.2\ 10^{-7}$	$4.3\ 10^{-13}$	$9.4\ 10^{-8}$	$3.0\ 10^{-12}$
20	0.50	0.5	92	88	63°	$1.1\ 10^{-10}$	$1.9\ 10^{-13}$	$1.4\ 10^{-10}$	$7.4\ 10^{-13}$
40	1.00	0.25	92	88	76°	$2.5\ 10^{-9}$	$1.4\ 10^{-13}$	$4.5\ 10^{-8}$	$1.9\ 10^{-13}$
100	1.00	0.25	212	208	76°	$1.0\ 10^{-9}$	$7.1\ 10^{-12}$	$6.1\ 10^{-9}$	$6.6\ 10^{-12}$
100	1.00	0.20	214	210	79°	$1.7\ 10^{-7}$	$7.7\ 10^{-12}$	$1.1\ 10^{-7}$	$6.8\ 10^{-12}$

ent $|\frac{\partial\varphi}{\partial n}|^{max} = |\varphi_n|^{max}$ on the free surface boundary ($z = 0$) (the maximum error $\varepsilon = -\log|\varphi_n|^{max}$ is also defined for conveniency of the diagrams). In case the adaptive integration is used for the 8 corner elements, results show the maximum errors always occur on the free surface, at the first node after the corner. In case the adaptive integration is not used, the maximum errors occur at some other location on the free surface.

Results in the corners themselves are modified during or after solution of Laplace's problem by imposing the compatibility conditions (22) or (26), (27). The accuracy in the corners is found excellent in all cases ($\mathcal{O}(10^{-15})$), which confirms the success of this operation.

Notice, finally, the average accuracy of the solution on the whole boundary closely follows the changes in magnitude of the maximum error ε. This shows the importance of an improved solution in the corner region on the global accuracy of the numerical solution. A detailed analysis of the results is presented in the following.

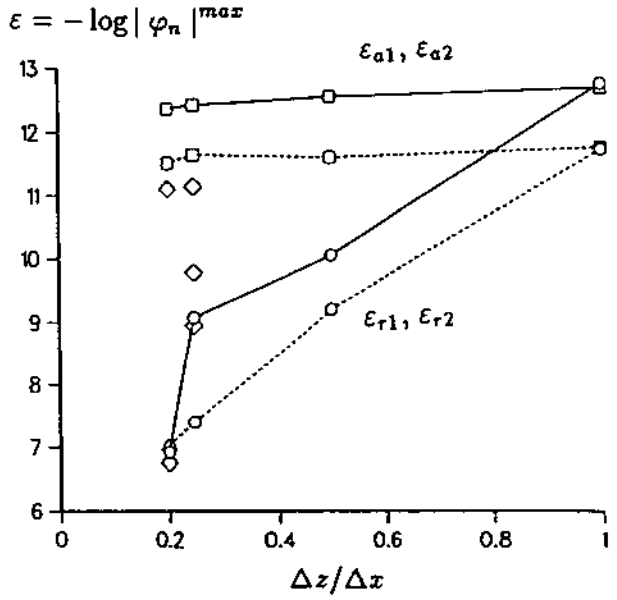

Fig. 3. Maximum error $|\varphi_n|^{max}$ of normal free surface gradient for problems 1 and 2 (Fig. 2), represented by $\varepsilon = -log|\varphi_n|^{max}$ (Table 3), as a function of the grid step ratio $\frac{\Delta z}{\Delta x}$: without adaptive integration ε_r (∘) or with adaptive integration ε_a (□), for $\frac{h}{d} = 10$ in problems 1 (——) or 2(- - - -). Results for $\frac{h}{d} = 100$ are represented by scattered (◇) symbols.

6.1.1. Effect of the numerical integrations on the accuracy of the solution

The effect of the numerical integrations over each element on the accuracy of the solution of both problems (1, 2), is studied in a first series of computations (Table 1). A square domain is selected, with $\frac{h}{d} = 1$, which eliminates the effects due to stretching the domain (investigated later) and the grid step is $\Delta x = \Delta z = 2$ ($\frac{\Delta x}{d} = 0.20$) with $N_\Gamma = 24$ and $M_\Gamma = 20$. The number of Gauss points (GP) in the integrations over each element is successively taken equal to 2, 4, 6, 8 and 10, and the adaptive integration is either used (subscript a) or not (subscript r) in the corner elements. For all these cases, the intercept angle in the corners is constant: $\alpha = 45°$ (i.e., the angle from which the corner element is seen from the first node on the other side of the corner). Without the adaptive integration, results in Table 1 show, ε_r varies roughly linearly with GP, between (3.2, 2.74) and (13.5, 13.0) in the first and second problems, respectively. With the adaptive integration, there is a gain of accuracy of 1 to 3 orders of magnitude.

Notice, results for the 1st problem ($a1$) are 2 to 3 times more accurate than those for the 2nd problem ($a2$). This will also be true in the majority of the cases studied later on.

6.1.2. Convergence of the solution

The convergence, or more exactly the non-divergence*, of the solution when the grid step $\Delta x = \Delta z$ is reduced, is checked in a square geometry with $\frac{h}{d} = 1$. This second series of computations is made in five different discretizations (Table 2), for both problems (1, 2). The number of GP is now fixed at 10 in all the computations. Results show the accuracy of the solution stays good for the smallest grid step ($\frac{\Delta x}{d} = 0.025$), though it slightly decreases with the grid step. This decrease is believed to be due to truncation errors in the integrations, which become larger when using many small elements. As could be expected from the higher grid density in the corners, the improvements due to the adaptive integration become less and less significant for small grid steps.

*The divergence of BEM solutions for refined grid steps has indeed often been pointed out in the literature.

6.1.3. Effect of horizontally stretching the geometry on the accuracy of the solution

To assess the effect of a horizontally distorted geometry on the accuracy of the solution, a third series of computations is made with the data in Table 3. The number of GP is still fixed at 10 in all the computations and both problems 1 and 2 are solved in each domain configuration. Two independent parameters are found to be responsible for the errors in the solutions, namely the grid step ratio $\frac{\Delta z}{\Delta x}$ (or maximum intercept angle α^{max}), and the domain aspect ratio $\frac{L}{d}$, the effects of which we want to analyze separately:

1. Five nodes at least must be kept on the lateral boundaries for calculating the s-derivatives in the wave model, which makes $\Delta z \leq \frac{d}{4}; \Delta x$, however, cannot be reduced accordingly, in order to limit the total discretization N_Γ to a reasonable size (maintaining $\Delta x = \Delta z$ would lead to a total discretization increasing like $(8\frac{L}{d} + 12)$). Therefore, when $\frac{L}{d}$ increases in practical applications (i.e., when d decreases for a fixed L in the present case), $\frac{\Delta z}{\Delta x}$, in general, has to decrease. Hence, the intercept angle α^{max} increases with larger $\frac{L}{d}$'s, leading to increasing losses of accuracy of the numerical integrations in the corners, in case the adaptive procedure is not used.
   The effect of a smaller $\frac{\Delta z}{\Delta x}$ (or of an increased α^{max}) on the accuracy of the solution is analyzed by selecting for the same aspect ratio $\frac{L}{d} = 10$ or 100, different grid step ratios (0.20 to 1.00). Results in Table 3 and in Fig. 3 show changes of 2 to more than 4 orders of magnitude for ε_{r1} or ε_{r2}, when the grid step ratio is reduced, whereas the ε_a's stay almost uninfluenced (the very slight increase observed in the error should only be due in this case to increased truncation errors in the integrations, because of smaller Δz). Clearly the adaptive integration removes most of the negative effects of reducing $\frac{\Delta z}{\Delta x}$.
2. Increasing the aspect ratio leads to both large and small geometric dimensions to be present in the computational domain ($L \gg d$), which corresponds to a large condition number of the BEM algebraic system matrix $\mathcal{H}_{ij}$. Hence, it is expected that truncation and round-off errors in the (direct) solution of the system should increase, making the overall accuracy of the solution decrease with $\frac{L}{d}$.
   The effect of increasing the aspect ratio $\frac{L}{d}$ is analyzed on cases calculated with the adaptive integration, in order to remove the effects of reducing $\frac{\Delta z}{\Delta x}$. Results in Table 3 and in Fig. 4 show ε_{a1} and ε_{a2} approximately linearly decrease with $\log \frac{L}{d}$. The accuracy, however, is still excellent up to $\frac{L}{d} = 100$ ($\mathcal{O}(10^{-11})$).

The role played by both parameters in all the results in Table 3 can be summarized the following way: the ε_r's are a monotonously increasing function of $\frac{\Delta z}{\Delta x}$, whereas the ε_a's do not show any clear correlation with it; hence the use of the adaptive integration removes the effect of reducing $\frac{\Delta z}{\Delta x}$ and improves the accuracy by 1 to more than 4 orders of magnitude. The horizontal stretching leads to a decrease in accuracy of 2 to 3 orders of magnitude, up to $\frac{L}{d} = 100$.

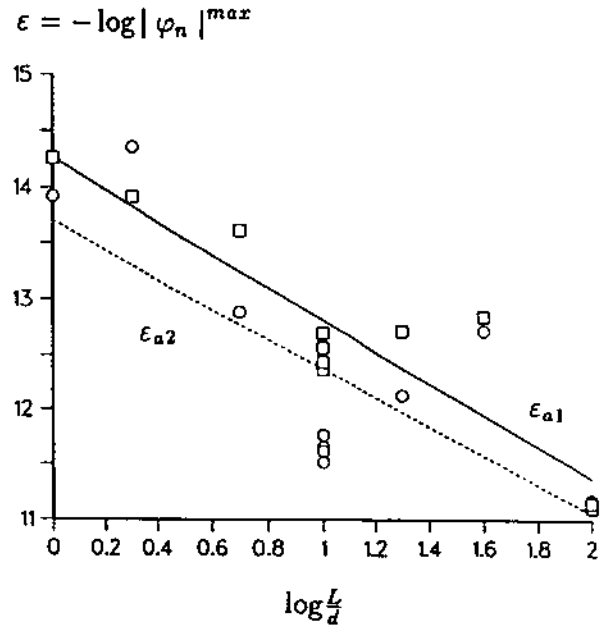

Fig. 4. Errors ε_{a1} (□) and ε_{a2} (○) (defined as in Fig. 3), as a function of the domain aspect ratio $\frac{L}{d}$. The effect of reducing $\frac{\Delta z}{\Delta x}$ from 1.00 to 0.20 in these computations, has been removed by using the adaptive integration. Linear fits to the ε_a's, in problems 1 (——) or 2 (- - - -), show approximate linear decrease with log $\frac{L}{d}$.

6.2. Global accuracy during propagation of an exact solitary wave

The examples in Section 6.1. assessed the effect on the accuracy of the solution of parameters such as: number of integration points per element, domain aspect ratio and grid step ratio. Computations made in a simple geometry showed that the adaptive integration procedure, used in the corner elements, removed the negative effects of reducing $\frac{\Delta z}{\Delta x}$. It was also shown, aspect ratios of up to 100 did not induce very significant losses of accuracy of the solution.

A more realistic case corresponding to the propagation over constant depth d of a fully nonlinear solitary wave, is now used to analyze the optimum relationship between Δx and Δt, with respect to the global accuracy of the results. An exact solitary wave, permanent wave solution of the fully nonlinear flow problem (1) to (4), is obtained by the method of Tanaka[32] and introduced in the BEM model by imposing its velocity potential on the free surface at initial time $t'_o = 0$ (by (5)). No-flux conditions ($u_c = \frac{\partial \phi}{\partial n} = 0$) are used on both lateral boundaries. Reflection of solitary waves by steep slopes and vertical walls has been studied in detail elsewhere (see Grilli and Svendsen[18]). Comparison with the experiments by Losada, *et al.*[25] also showed very good agreements with the computational results (Grilli and Svendsen[16,18]).

A steep wave of $H' = 0.5$ is propagated by the BEM model during 5 time units, i.e., over a horizontal distance of theoretically $5c'$ (depths). Constancy during wave propagation of the dimensionless volume m of the wave (above $z = 0$), total energy e_t, wave shape and celerity, is used to check the accuracy of the computations. Tanaka's solution provides for $H' = 0.5$: $m = 1.79148$, $e_t = 0.615712$, and $c' = 1.21578$ (primes denote dimensionless variables defined as in Section 5.2.). The domain aspect ratio is $\frac{L}{d} = 28$ (with $d = 1$), and the initial wave is truncated left and right with $\varepsilon_z = 5\,10^{-6}$ (see Section 5.2.)

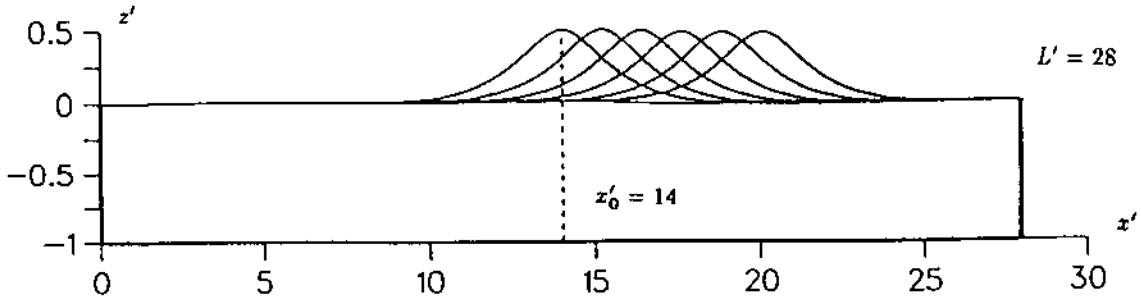

Fig. 5. Free surface profiles for the propagation over constant depth of an exact solitary wave of height $H' = 0.5$, during 5 units of time from time $t' = 0$ to 5, shown by steps of 1 (i.e. over ~ 6.08 units of length). Length of the domain is $L' = 28$ and the initial position of the crest is $x'_o = 14$. Notice vertical scale has been exagerated 4 times. Results for various space and time discretizations are given in Table 5 and in Fig. 6.

and introduced in the model at $t'_o = 0$, with its maximum amplitude at $x'_o = 14$. Figure 5 shows initial and last computed wave profiles; one sees, reflection is negligible over the propagation distance considered.

Three spatial discretizations are used in the computations, with free surface grid steps $\Delta x' = \frac{\Delta x}{d}$ (0.15, 0.20, 0.25); in each discretization, $\Delta z' = 0.25$ on the lateral boundaries; $\Delta x'$ is 0.25 on the bottom, in the first set of results and 0.40 in the next two ones. Quasi-spline elements in number $M_f \sim \frac{L'}{\Delta x'}$ are used on the free surface, and three-node quadratic elements on the three other boundaries. Adaptive integration is used in the corner elements, and 10 GP are used per element. Table 4 summarizes data for the three discretizations. The CPU time provided is per time step on an IBM 3090/300, including a printing and saving time of about 10%. Results in the last two columns of Table 4 are the volume and total energy changes at the very first time step of the propagation, with respect to Tanaka's theoretical values. They are time step independent and reflect the little adjustments undertaken by the wave, calculated by Tanaka's Cauchy theorem method, when introduced in the discretized BEM model. Whereas volume is found identical to within $2.85\ 10^{-4}$ % somewhat independently of $\Delta x'$, the total energy is found identical to within $2.85\ 10^{-2}$ % in the most refined grid.

Four different time steps $\Delta t'$ (temporal discretization) are used in each discretization (0.025, 0.05, 0.10, 0.20), which corresponds to propagating the solitary wave over 201, 101, 51 or 26 time steps respectively (or 33.0, 16.5, 8.4, or 4.2 time steps per water depth of propagation). Hence 12 different propagation problems are calculated.

Table 4. Discretization data for the propagation over constant depth of an exact solitary wave of height $H' = \frac{H}{d} = 0.5$: $\Delta x' = \frac{\Delta x}{d}$ is the horizontal step between nodes on the free surface; there are N_Γ nodes and M_Γ elements: M_f 2-node quasi-splines on the free surface and $M = M_\Gamma - M_f$ 3-node quadratic elements elsewhere. The CPU is per time step (IBM 3090/300) and the Δ^T's are the differences between the calculated values for the wave at the first time step with respect to Tanaka's[12] theoretical volume $m = 1.79148$ and total energy $e_t = 0.615712$.

$\Delta x'$	N_Γ	M_Γ	M_f	CPU(s)	$\Delta^T m$	$\Delta^T e_t$
0.25	236	178	112	2.67	$-5.30\ 10^{-6}$	$-5.02\ 10^{-4}$
0.20	222	179	140	2.45	$-5.20\ 10^{-6}$	$-3.16\ 10^{-4}$
0.15	268	225	186	3.73	$-5.10\ 10^{-6}$	$-1.76\ 10^{-4}$

Results in Table 5 show the maximum differences (Δ^*) found between the calculated value during wave propagation between $t'_o = 0$ and $t' = 5$, and the values at t'_o, as a function of the spatial and temporal discretizations. They are of two natures: changes in amplitude $\Delta^* H'$ and celerity $\Delta^* c'$ which are "one point results" (i.e., measured at one point of the wave), and changes in volume $\Delta^* m$ and total energy $\Delta^* e_t$ which are "boundary integrated" results (see Grilli, *et al.*[13], for the calculation of m and e_t by boundary integral). Figures 6(a) and (b) show logarithmic diagrams of these results, two by two, as a function of $\Delta x'$ and of the Courant number (CLF) defined as $\frac{\Delta t'}{\Delta x'}$ (also given in Table 5).

Figure 6(a) shows, the errors of the "one point results" reduce with the Courant number until they reach a minimum error for $\frac{\Delta t'}{\Delta x'} \leq 0.5$. For a constant $\Delta x'$, results do not improve further when reducing the time step; errors can only be decreased by reducing $\Delta x'$. One also sees, errors roughly increase with the cube of the Courant number, for $\frac{\Delta t'}{\Delta x'} > 0.5$, i.e., with $\sim \Delta t'^3$, for constant $\Delta x'$, as could be expected from the truncation error in the second order Taylor series used in the time integration. Figure 6(b) shows, the "integrated results" follow a similar pattern, with a minimum of the error reached in most of the cases around $\frac{\Delta t'}{\Delta x'} = 0.3 - 0.5$; this minimum error, again, only decreases with $\Delta x'$. Reducing the Courant number further makes the errors even slightly

Table 5. Checks on accuracy for the propagation over constant depth of an exact solitary wave of height $H' = \frac{H}{d} = 0.5$ during 5 time units: $\Delta x'$ is the horizontal step between nodes on the free surface, $\Delta t'$ is the time step and $\frac{\Delta t'}{\Delta x'}$ the Courant number; the Δ^*'s are the maximum differences between the calculated values for the wave propagation between $t'_o = 0$ and $t' = 5$, and the values at the first time step for: the amplitude H', celerity c', volume m and total energy e_t

$\Delta x'$	$\Delta t'$	$\frac{\Delta t'}{\Delta x'}$	$\Delta^* H'$	$\Delta^* c'$	$\Delta^* m$	$\Delta^* e_t$
0.25	0.20	0.80	$4.60\ 10^{-3}$	$2.06\ 10^{-2}$	$-6.78\ 10^{-4}$	$2.33\ 10^{-4}$
0.25	0.10	0.40	$2.29\ 10^{-3}$	$3.29\ 10^{-3}$	$-2.70\ 10^{-4}$	$-3.96\ 10^{-4}$
0.25	0.05	0.20	$2.03\ 10^{-3}$	$2.95\ 10^{-3}$	$-2.85\ 10^{-4}$	$-5.10\ 10^{-4}$
0.25	0.025	0.10	$2.01\ 10^{-3}$	$2.87\ 10^{-3}$	$-3.06\ 10^{-4}$	$-5.51\ 10^{-4}$
0.20	0.20	1.00	$2.04\ 10^{-2}$	$3.50\ 10^{-2}$	$-1.02\ 10^{-3}$	$4.80\ 10^{-4}$
0.20	0.10	0.50	$1.63\ 10^{-3}$	$1.41\ 10^{-3}$	$-1.95\ 10^{-4}$	$-2.41\ 10^{-4}$
0.20	0.05	0.25	$1.20\ 10^{-3}$	$1.06\ 10^{-3}$	$-1.85\ 10^{-4}$	$-3.43\ 10^{-4}$
0.20	0.025	0.13	$1.11\ 10^{-3}$	$9.80\ 10^{-4}$	$-1.97\ 10^{-4}$	$-3.70\ 10^{-4}$
0.15	0.20	1.33	$1.19\ 10^{-1}$	$-8.46\ 10^{-2}$	$-1.33\ 10^{-2}$	$4.08\ 10^{-2}$
0.15	0.10	0.67	$1.13\ 10^{-3}$	$3.37\ 10^{-3}$	$-1.35\ 10^{-4}$	$-1.12\ 10^{-4}$
0.15	0.05	0.33	$7.20\ 10^{-4}$	$5.70\ 10^{-4}$	$-1.09\ 10^{-4}$	$-1.98\ 10^{-4}$
0.15	0.025	0.17	$6.80\ 10^{-4}$	$4.90\ 10^{-4}$	$-1.14\ 10^{-4}$	$-2.17\ 10^{-4}$

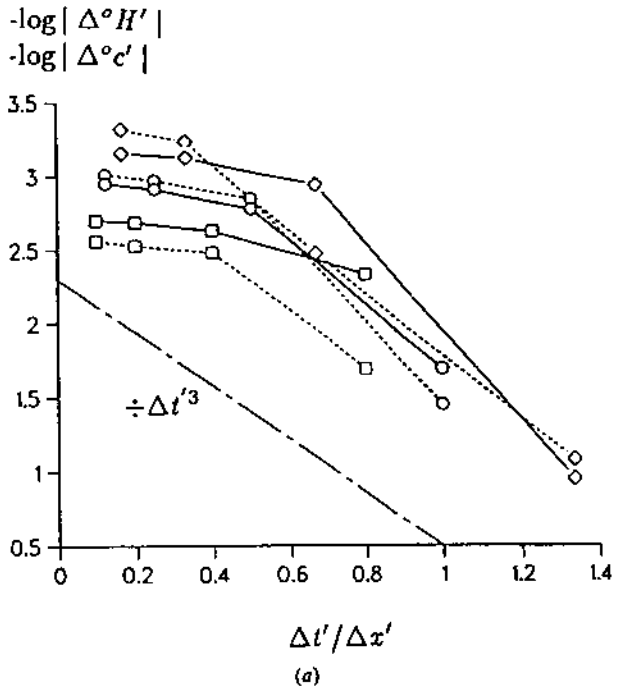

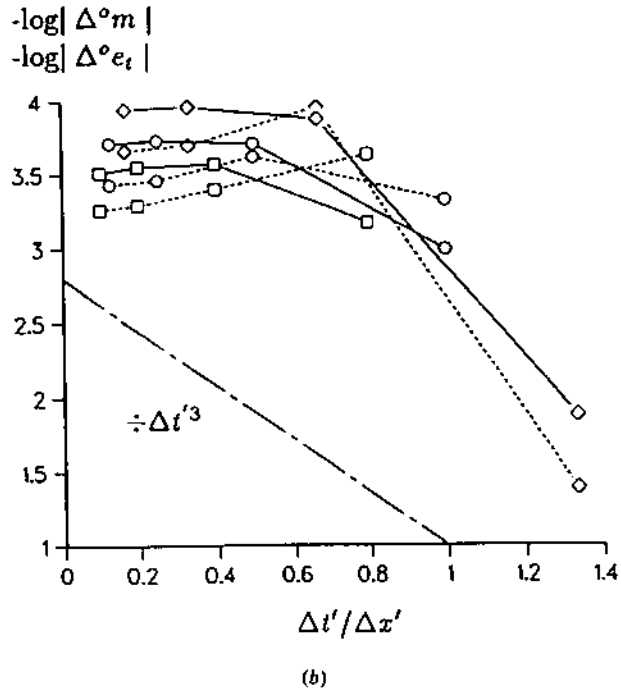

Fig. 6(a). "One point" numerical errors for the case in Fig. 5, as absolute maximum differences with the initial values during propagation ($-\log(|\Delta^\circ|)$ for: the changes in wave height $\Delta^\circ H'$ (——) and celerity $\Delta^\circ c'$ (- - - -), as a function of the Courant number $\mathscr{C}_o = \frac{\Delta t'}{\Delta x'}$. Results are for three horizontal grid steps $\Delta x' = 0.25$(□), 0.20 (∘) and 0.15 (◇). Theoretical truncation error is shown $\sim \Delta t'^3$ (— - — - —) for an arbitrary constant grid step. Notice results do not improve for $\mathscr{C}_o < 0.5$. Fig. 6(b). "Boundary integrated" numerical errors for the case in Fig. 5, with the same horizontal grids and definitions as in Fig. 6(a), for: the changes in volume $\Delta^\circ m$ (——) and total energy $\Delta^\circ e_t$ (- - - -) of the wave. Notice results are optimum around $\mathscr{C}_o = 0.3 - 0.7$.

worse likely due to the accumulation of truncation errors (somewhat more significant here because of the integration along the boundary), when using unnecessary large numbers of time steps. For larger Courant numbers, the errors again increase as $\sim \Delta t'^3$ or slightly greater.

In conclusion, high accuracy ($\mathcal{O}(10^{-4})$) can be achieved for a solitary wave of $H' = 0.5$ with an optimum Courant number around $\frac{\Delta t'}{\Delta x'} = 0.5$ (notice, this also corresponds to the theoretical optimum CLF number). In this case, refining the spatial discretization always reduces the errors further. Notice, however, quite small errors are already obtained with slightly larger Courant numbers and rather coarse discretizations, like for instance in the case of the first line of Table 5 with $\frac{\Delta t'}{\Delta x'} = 0.8$ and $\Delta x' = 0.25$, which only corresponds to four nodes per water depth on the free surface, and 4.2 time steps for the propagation of the wave over one water depth.

An optimum Courant number around 0.5 should also be valid for other waves of simple shape with similar celerity, by making it proportional to the celerity of the wave or of the water particles. When rapidly changing local phenomena are involved, however, like in the tip of a breaking wave or during wave runup-rundown on a structure, convergence of nodes by Lagrangian motion is observed, which locally reduces $\Delta x'$ and also somewhat increases the partical velocities. Hence, it is expected that, even though the local optimum Courant number should stay around 0.5, a much smaller number, based on the original $\Delta x'$ should be selected. At best, an auto-adaptive time stepping, maintaining constant the Courant number based on the smaller node interval should be implemented and used (see Section 6.3.).

6.3. Global accuracy during generation of wave overturning by a piston wave-maker

The generation of overturning waves by a piston wavemaker is calculated to illustrate and check the accuracy of the continuity and compatibility conditions at the intersection between the free surface and a moving lateral boundary (Section 4.3.). Adaptive integration is used in the corner elements (10 GP per element) and, due to wave breaking, it is also selectively used on parts of the tip of the overturning wave, where the proximity of two sections of the boundary would otherwise lead to a loss of accuracy.

Following the analysis in Section 4.1., a piston motion with very small initial acceleration is selected. The law of motion (34), (35) (Section 5.2.), which has been used in other studies for generating first-order solitary waves over constant depth d (Grilli, *et al.*[12–18]), provides a small initial wavemaker acceleration and has a relatively large maximum acceleration at the mid part of the motion (required for generating wave overturning). The initial acceleration is deduced from (36) as $\ddot{u}'_p(0) \simeq \sqrt{3}\, H'^{3/2}(1 + H')\varepsilon_z$. Exact solitary waves are known to become unstable for $H' \simeq 0.78$ (Tanaka[32,33]). Thus, introducing much higher H' in (34), (35) creates a wave which rapidly breaks quite close to the wavemaker. This gives us a strong test for both the corner treatment and the accuracy of the integrations.

A wave with height $H' = 2$ ($\varepsilon_z = 0.002$ and $c' \simeq 1.73$) is generated in a tank of length $L' = \frac{1}{2}$. Although the wavemaker accelerates up to $\ddot{u}'^{max}_p = 0.96$ in this case, the initial acceleration is only: $\ddot{u}'_p(0) \simeq 0.0294$. Two spatial

discretizations are used with quasi-spline elements on the free surface and 2-node elements elsewhere: A first one with $L' = 10, \Delta x' = 0.25$ for the initial discretization on the free surface and on the bottom and $\Delta z' = 0.125$ on the lateral boundaries ($N_\Gamma = 96$ and $M_\Gamma = 92$). A second one with $L' = 8$ and $\Delta x' = \Delta z' = 0.10$ ($N_\Gamma = 179$ and $M_\Gamma = 175$). With these data, CPU times per time step are 0.79 and 1.90s respectively (IBM 3090/300).

To account for the large variations in the distance between nodes, induced by the Lagrangian motion, an auto-adaptive time stepping is implemented, based on the conclusions in Section 6.2. The minimum distance $\Delta|\mathbf{r}'|^{min}$ between nodes on the free surface is used to determine, for each time, a new time step ensuring an optimum ratio $\frac{\Delta t'}{\Delta x'^2}$ in the computations as: $\Delta t' = \Delta|\mathbf{r}'|^{min}\mathscr{C}_o$, with $\mathscr{C}_o = \frac{\Delta t'_o}{\Delta x'^2}$, the Courant number at initial time t'_o. An estimate of the optimum Courant number is obtained from Section 6.2 by: $\mathscr{C}_o = 0.5 \times 1.22/1.73 \simeq 0.35$ (proportionally to the celerity). Three cases are considered with different Courant numbers and initial time steps: $\mathscr{C}_o = 0.32$ and 0.16 in the coarsest discretization, i.e., $\Delta t'_o = 0.08$ and 0.04, and $\mathscr{C}_o = 0.40$ in the finest discretization, i.e., $\Delta t'_o = 0.04$.

Figures 7(a), (b) and (c) show dimensionless free surface elevations z' (of x') for the three considered cases. The wavemaker is located, for each time, at the leftward extremity of the free surface. We see, the free surface geometry around the intersection with the wavemaker stays very smooth during the motion; this is also true for the variation of ϕ, $\frac{\partial\phi}{\partial n}$, $\frac{\partial\phi}{\partial t}$ and $\frac{\partial^2\phi}{\partial t\partial n}$ not shown on the figures.

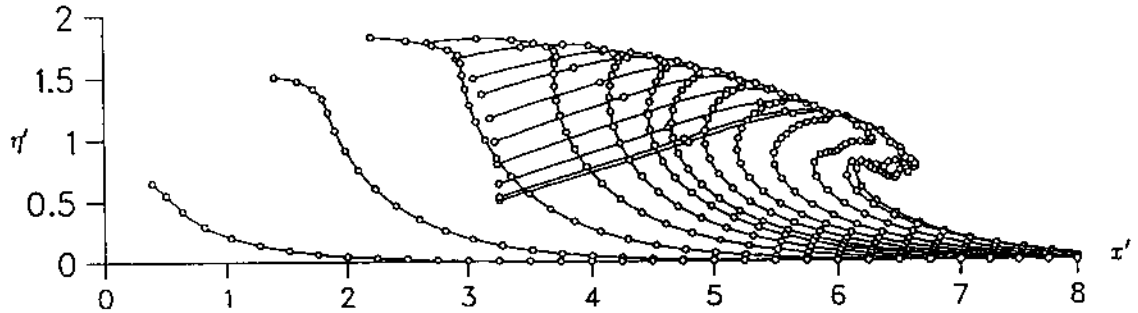

Fig. 7(a). Dimensionless free surface profiles shown each 25 time steps (at t' = 1.55, 2.53, 3.25, 3.69, 3.97, 4.19, 4.32, 4.51, 4.68, 4.86, 5.04, 5.18, 5.22) for an overturning wave generated by a 1st-order solitary wave piston motion, with H' = 2.0. Auto-adaptive time stepping is used with $\mathscr{C}_o = 0.32$ for $\Delta x' = 0.25$ ($\Delta t'$ varies from 0.08 to 0.0004, $\Delta z' = 0.125$ and $L' = 10$). The circles denote nodes-fluid particles. Notice computations break down shortly after the last profile.

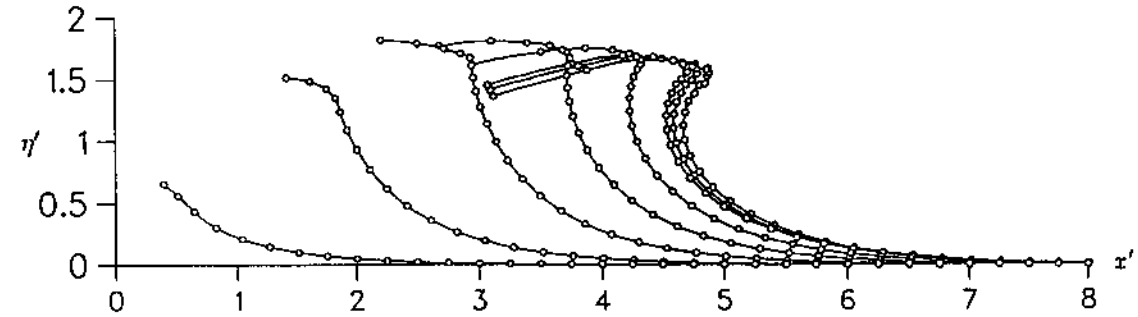

Fig. 7(b). Same definitions as in Fig. 7(a) with $\mathscr{C}_o = 0.16$ ($\Delta t'$ is 0.04 to 0.0003). Profiles are shown each 50 time steps (at t' = 1.56, 2.55, 3.24, 3.70, 4.02, 4.23, 4.27, 4.33). Notice computations break down shortly after the last profile.

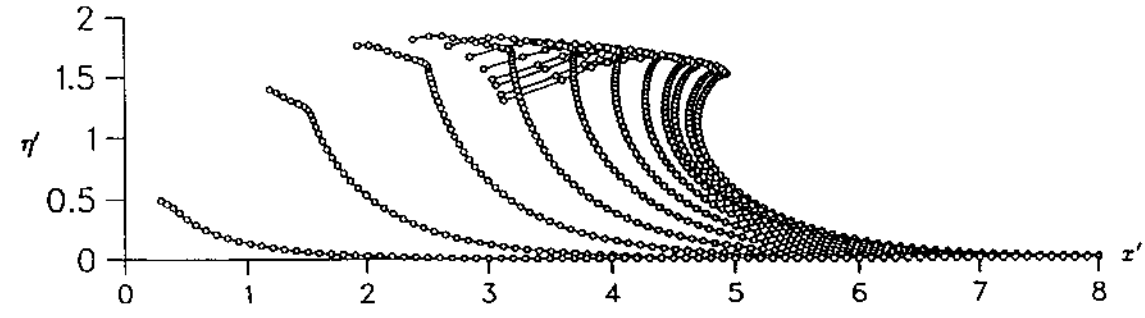

Fig. 7(c). Same definitions as in Fig. 7(a) with $\mathscr{C}_o = 0.40$ for $\Delta x' = 0.10$ ($\Delta t'$ varies from 0.04 to 0.0002, $\Delta z' = 0.10$ and $L' = 8$). Profiles are shown each 50 time steps (at t' = 1.41, 2.35, 2.99, 3.41, 3.71, 3.90, 4.05, 4.16, 4.22, 4.30, 4.34). Notice computations break down shortly after the last profile.

The small circles represent nodes of the discretization, identical to the free surface particles, whose Lagrangian motion is followed in time. Surface profiles are given at different dimensionless times t' corresponding to intervals of 25, 50 and 50 (varying) time steps, in each case respectively. Hence, the distance between two profiles gives a measure of the change in size of the time step ($\Delta t'$ reduces down to 0.0004, 0.0003 and 0.0002 respectively at the time of the last computed profile), and the corresponding total number of time steps is 323, 405 and 550 in each case. Computations are pursued up to the time wave has overturned and the strong convergence of the flow in the tip of the wave concentrates the fluid particles so much that it creates a quasi-singular situation. Neither the auto-adaptive time stepping nor the adaptive integration can handle this well and computations eventually breakdown shortly after the last profile shown in each of the figures. Clearly regriding of the nodes should be done to be able pursuing the computations further in time (see Dommermuth and Yue[6]).

Analyzing results in more detail, we see that, in the first two cases with same discretization (Fig. 7(a), (b)), reducing $\mathscr{C}_o$ makes the computations fail earlier: at $t' = 4.326$ with $\mathscr{C}_o = 0.16$, instead of $t' = 5.223$ with $\mathscr{C}_o = 0.32$. In Figure 7b, this is likely due to an accumulation of truncation errors with an unnecessary large number of time steps, which makes nodes (wrongly) move too close to each other. In Fig. 7(a), computations can be pursued accurately till almost complete overturning of the wave. Notice, the intervals between nodes close to the wavemaker become quite wide. This is well handled, however, by both the cubic splines approximation of the free surface and by the adaptive integration. In Fig. 7(c), computations fail around the same time as in Fig. 7(b) ($t' = 4.344$ with $\mathscr{C}_o = 0.40$), likely due here to the more refined discretization which brings nodes closer to each other at the tip of the wave and eventually leads to numerical instability.

Overall accuracy is compared between the three cases by checking the conservation of the initial volume ($V = 10$ and 8 for the first two and for the third case respectively). In Fig. 7(d), a plot of the change in volume $\Delta^o V$ as a function of time is shown for the three cases. We see, accuracy increases from case 1 to 3 and, up to $t' = 4$, the maximum volume error is -0.0073, -0.0065 and -0.0008 respectively. As expected, reducing $\mathscr{C}_o$ from 0.32 to 0.16 in the same discretization does not bring much accuracy (10%), whereas reducing $\Delta x'$ from 0.25 to 0.10 decreases the maximum error by 89%. At later times, the maximum error increases up to $\Delta^o V = 0.0561, 0.0029$ and 0.0080 respectively for the last computed profile.

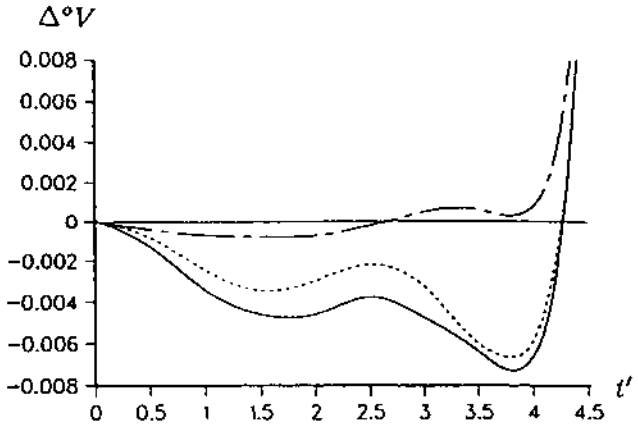

Fig. 7(d). Volume change $\Delta^o V(t')$ during computations, for the three cases in Fig. 7(a) (——), 7b (- - - -) and 7c (— - — -). Notice initial volume is $V = 10$ (7(a), 7(b)) and 8 (7c).

In Fig. 8, the free surface profiles of cases 1 and 3 are compared at identical times ($t' = 1.18$ to 3.58 by steps of 0.40). The overall agreement is excellent, which provides a good proof of the convergence of the method in this case. Slight differences only show up in small portions at the back and at the tip of the wave, corresponding to elements with either very small (case 3) or too large (case 1) intervals between nodes, which leads to less accurate integrations and BEM solution.

Some quite interesting hydrodynamic features in Fig. 7(a) should finally be pointed out. Maximum amplitude increases on the free surface up to the time where there is a vertical tangent at the front face of the wave ($H' \simeq 1.83$ at $t' = 3.692$). This also roughly corresponds to the time of largest (negative) acceleration of the wavemaker. Then, the wave starts overturning and its maximum amplitude decreases smoothly and continuously until the wave eventually collapses on itself. This can be explained by the combination of both a strong downward velocity of the particles, due to the transfor-

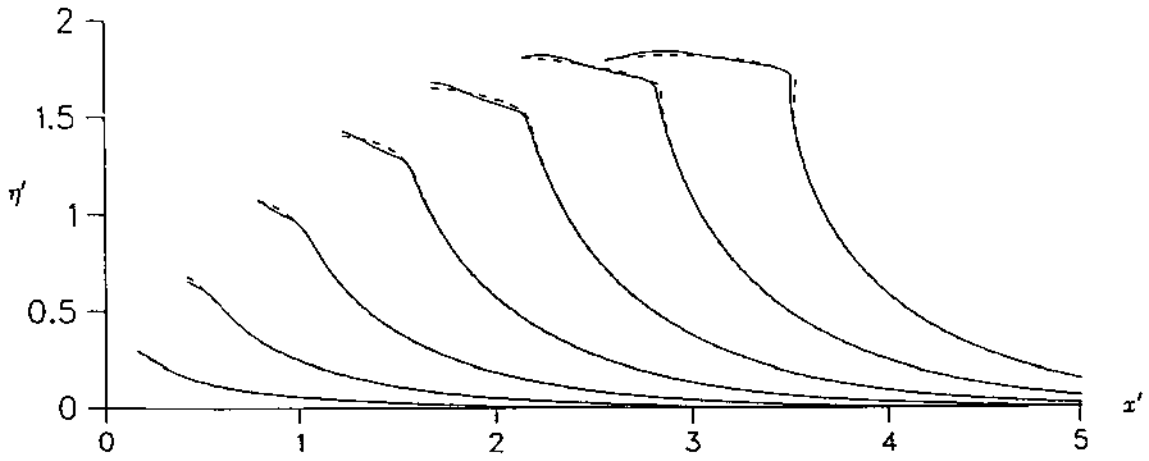

Fig. 8. Comparison between results in case 7(a) (- - - -) and 7(c) (——), for $t' = 1.18$ to 3.58, by 0.40.

mation of potential energy gained during the building up of the wave height, and of large horizontal velocities and accelerations directly gained from the wavemaker motion. Eventually, the tip of the overturning wave becomes elongated enough in the horizontal direction, for a little body of water to be expelled downwards, out of its side. This creates some sort of "bimodal" plunging breaker.

7. CONCLUSIONS

We identified five separate aspects of the corner treatment, relevant when solving wave problems with the BEM in the physical space, and we addressed the associated problems separately, leading to an improved corner solution.

Applications of the nonlinear wave model to simple examples with analytic solution, using the improved corner solution, demonstrate substantial gains in accuracy and stability of the overall solution. Cases with different horizontal and vertical grid steps in the discretization, large horizontal aspect ratio of the domain geometry, and mixed boundary conditions (of all possible kinds) are well handled in the model. The representation of the corners by double-nodes, with imposition of continuity and compatibility conditions, provides well-posed mixed boundary conditions in all cases. The use of an adaptive integration in the corner elements (and also on any part of the boundary with large intercept angle) reduces by several orders of magnitude, the loss of accuracy of the corner solution often mentioned in the literature.

The optimum relationship between space and time discretization, leading to maximum accuracy of the results, has been deduced for the propagation over constant depth of an exact solitary wave. It is expressed as a Courant number $\mathscr{C}_o = \frac{\Delta t_o}{\Delta x} = \frac{\Delta t_o}{\Delta x}\sqrt{gd}$ whose optimum value is within 0.3-0.5 (when $\sqrt{gd} \sim 1.7$-1.2). The accuracy of the solution at the corner between free surface and moving lateral boundary is studied for the generation of an overturning wave by a piston wavemaker. This leads to using an auto-adaptive time stepping, based on maintaining constant the Courant number derived with the minimum distance between nodes on the free surface: $\Delta t' = \Delta|\mathbf{r}'|^{min}\mathscr{C}_o$. Results show interesting hydrodynamic features of wavemaker induced overturning of a wave.

REFERENCES

1. Brebbia, C. A. *The Boundary Element for Engineers.* John Wiley & Sons, U.K., 1978
2. Cointe, R. Remarks on the numerical treatment of the intersection point between a rigid body and a free surface. In *Proc. 3rd Intl. Workshop on W. Waves and Fl. Bodies, Woods Hole–MA*, 1988
3. Cointe, R. Quelques aspects de la simulation numérique d'un canal à houle. *Thèse de Docteur de l'Ecole Nationale des Ponts et Chaussées*, 1989, 284 pps
4. Cointe, R., Jami, A. and Molin, B. Nonlinear impulsive problems. In *Proc. 2nd Intl. Workshop on W. Waves and Fl. Bodies, Bristol UK*, 1987
5. Dold, J. W. and Peregrine, D. H. An efficient Boundary Integral Method for steep unsteady water waves. *Numerical methods for Fluid Dynamics II* (ed. K. W. Morton & M. J. Baines), 1986, 671-679. Clarendon Press, Oxford
6. Dommermuth, D. G. and Yue, D. K. P. Numerical simulation of nonlinear axisymmetric flows with a free surface. *J. Fluid Mech.* 1987, 178, 195-219
7. Goring D. G. Tsunamis- The propagation of long waves onto a shelf. *W. M. Keck Laboratory of Hydraulics and Water Resources, California Institute of Technology, Report No. KH-R-38*, 1978
8. Greenhow, M. and Lin, W. M. Numerical simulation of nonlinear free surface flows generated by wedge entry and wave-maker motions. In *Proc. 4th Intl. Conf. on Numerical Ship Hydrody., Washington, USA*, 1985
9. Greenhow, M. and Lin, W. M. The interaction of nonlinear free surfaces and bodies in two dimensions. *MARTINTEK, Report No. OR/53/530030.12/01/86*, 1986, 36 pps
10. Gray, L. J. Numerical experiments with a Boundary Element technique for corners. *Advances in Boundary Elements* (Proc. 11th Intl. Conf. on Boundary Elements, Cambridge, Massachusetts, USA), Vol. 1 (ed. C. A. Brebbia, J. J. Connor), 243-251. Computational Mechanics Publication. Springer Verlag, Berlin, 1989
11. Grilli, S. Etude de l'action de la houle sur les structures flottantes par éléments frontières. Comparaison avec les éléments finis. *Bulletin de l'ATMA*, 1984, 84, 297-318
12. Grilli, S., Skourup, J. and Svendsen, I. A. The modelling of highly nonlinear waves: A step toward the numerical wave tank. Invited paper in *Proc. 10th Intl. Conf. on Boundary Elements, Southampton, England*, Vol. 1 (ed. C. A. Brebbia), pp. 549-564. Computational Mechanics Publication. Springer Verlag, Berlin, 1988
13. Grilli, S., Skourup, J. and Svendsen, I. A. An Efficient boundary element method for nonlinear water waves. *Engineering Analysis with Boundary Elements*, 1989, 6(2), 97-107
14. Grilli, S. and Svendsen, I. A. The modelling of nonlinear water wave interaction with maritime structures. *Advances in Boundary Elements* (Proc. 11th Intl. Conf. on Boundary Elements, Cambridge, Massachusetts, USA), Vol. 2 (ed. C. A. Brebbia, J. J. Connor), 253-268. Computational Mechanics Publication. Springer Verlag, Berlin, 1989
15. Grilli, S. and Svendsen, I. A. The modelling of highly nonlinear waves. Part 2: Some improvements to the numerical wave tank. *Advances in Boundary Elements* (Proc. 11th Intl. Conf. on Boundary Elements, Cambridge, Massachusetts, USA), Vol. 2 (ed. C. A. Brebbia, J. J. Connor), pp. 269-281. Computational Mechanics Publication. Springer Verlag, Berlin, 1989
16. Grilli, S. and Svendsen, I. A. Computation of nonlinear wave kinematics during propagation and runup on a slope. *Water Wave Kinematics*, (Proc. NATO-ARW, Molde, Norway, May 89) (ed. A. Torum & O. T. Gudmestad *NATO ASI Series E: Applied Sciences*, 1990, 178, 297-312. Klüwer Academic Publishers
17. Grilli, S. and Svendsen, I. A. Wave interaction with steeply sloping structures. To be published in *Proc. 22nd Intl. Conf. on Coastal Engineering* (ICCE22, Delft, The Netherland, July 90). ASCE edition, 1990
18. Grilli, S. and Svendsen, I. A. The runup and reflection of solitary waves on steep slopes. Submitted to *J. Fluid Mech.*, 1990
19. Grilli, S., Svendsen, I. A. and Otta, A. K. Corner effects using BEM for nonlinear waves. Computational Engineering with Boundary Elements. *(Proc. 5th Intl. Conf. on Boundary Element Technology, Newark, Delaware, USA)* (ed. S. Grilli, C. A. Brebbia & A. H. Cheng), Vol. 1, pp. 101-118. Computational Mechanics Pub., Southampton, 1990
20. Klopman, G. Numerical simulation of gravity wave motion on steep slopes. *Delft Hydraulics Report No. H195*, 1988
21. Kravtchenko, J. Remarques sur le calcul des amplitudes de la houle linéaire engendrée par un batteur. In *Proc. 5th Intl. Conf. on Coastal Engineering*, 1954, pp. 50-61
22. Lin. W. M. *Nonlinear Motion of the Free Surface Near a Moving Body* (Ph.D. Dissertation), MIT, Cambridge-MA, 1984
23. Lin, W. M., Newman, J. N. and Yue, D. K. Nonlinear forced motion of floating bodies. In *Proc. 15th Intl. Symp. on Naval Hydrody., Hamburg, Germany*, 1984
24. Longuet-Higgins, M. S. and Cokelet, E. D. The deformation of steep surface waves on water—I. A numerical method of computation. *Proc. R. Soc. Lond.*, 1976, A350, 1-26
25. Losada, M. A., Vidal, C. and Nunez, J. Sobre el comportamiento de ondas propagádose por perfiles de playa en barra y diques sumergidos. *Dirección General de Puertos y Costas Programa de Clima Maritimo. Universidad de Cantábria. Publicación No. 16*, 1986
26. Peregrine, D. H. Flow due to a vertical plate moving in a channel. *Unpublished Notes*, 1972
27. Roberts, A. J. Transient free-surface flows generated by a moving vertical plate. *Q. J. Mech. Appl. Math.*, 1987, 40(1), 129-158
28. Romate, J. E. *The numerical simulation of nonlinear gravity waves in three dimensions using a higher order panel method* (Ph.D. Dissertation), Delft Hydraulics, The Netherlands, 1989

29. Seo, S. N. *Time-Dependent Highly Nonlinear Waves* (Ph.D. Dissertation). *Civil Engineering Department, University of Delaware, U.S.A.*, 1988
30. Svendsen, I. A. and Grilli, S. Nonlinear waves on steep slopes. *J. Coastal Research*, 1990, SI 7 1-18
31. Tanaka, M., Dold, J. W., Lewy, M. and Peregrine, D. H. Instability and breaking of a solitary wave. *J. Fluid Mech.* 1987, **185**, 235-248
32. Tanaka, M. The stability of solitary waves. *Phys. Fluids*, 1986, **29**(3), 650-655
33. Vinje, T. and Brevig, P. Numerical simulation of breaking waves. *Adv. Water Resources*, 1981, **4**, 77-82